

Whitecap Coverage Dependence on Wind and Wave Statistics as Observed during SO GasEx and HiWinGS

SOPHIA E. BRUMER,^a CHRISTOPHER J. ZAPPA,^a IAN M. BROOKS,^b HITOSHI TAMURA,^c
SCOTT M. BROWN,^a BYRON W. BLOMQUIST,^{d,e} CHRISTOPHER W. FAIRALL,^d
AND ALEJANDRO CIFUENTES-LORENZEN^f

^a *Ocean and Climate Physics Division, Lamont-Doherty Earth Observatory, Columbia University, Palisades, New York*

^b *School of Earth and Environment, University of Leeds, Leeds, United Kingdom*

^c *Port and Airport Research Institute, Yokosuka, Japan*

^d *National Oceanic and Atmospheric Administration/Earth System Research Laboratory, Boulder, Colorado*

^e *Cooperative Institute for Research in Environmental Sciences, University of Colorado Boulder, Boulder, Colorado*

^f *Department of Marine Sciences, University of Connecticut, Groton, Connecticut*

(Manuscript received 6 January 2017, in final form 21 June 2017)

ABSTRACT

Concurrent wavefield and turbulent flux measurements acquired during the Southern Ocean (SO) Gas Exchange (GasEx) and the High Wind Speed Gas Exchange Study (HiWinGS) projects permit evaluation of the dependence of the whitecap coverage W on wind speed, wave age, wave steepness, mean square slope, and wind-wave and breaking Reynolds numbers. The W was determined from over 600 high-frequency visible imagery recordings of 20 min each. Wave statistics were computed from in situ and remotely sensed data as well as from a WAVEWATCH III hindcast. The first shipborne estimates of W under sustained 10-m neutral wind speeds U_{10N} of 25 m s^{-1} were obtained during HiWinGS. These measurements suggest that W levels off at high wind speed, not exceeding 10% when averaged over 20 min. Combining wind speed and wave height in the form of the wind-wave Reynolds number resulted in closely agreeing models for both datasets, individually and combined. These are also in good agreement with two previous studies. When expressing W in terms of wavefield statistics only or wave age, larger scatter is observed and/or there is little agreement between SO GasEx, HiWinGS, and previously published data. The wind speed-only parameterizations deduced from the SO GasEx and HiWinGS datasets agree closely and capture more of the observed W variability than Reynolds number parameterizations. However, these wind speed-only models do not agree as well with previous studies than the wind-wave Reynolds numbers.

1. Introduction

Whitecaps are the surface signature of air-entraining breaking waves consisting of subsurface bubble clouds and surface foam patches. They have been studied extensively since the late 1960s because of the role of bubbles in the air-sea exchange of gases, and the production of sea spray aerosols. They form under wind speeds as low as 3 m s^{-1} (Hanson and Phillips 1999; Monahan and O'Muircheartaigh 1986) and have been estimated to cover, on average, 1%–4% of the global oceans (Blanchard 1963, 1983). Their high albedo makes

them easily detectable locally with cameras set up on stable platforms (e.g., Callaghan et al. 2008a; Lafon et al. 2007, 2004; Sugihara et al. 2007) as well as from ships (e.g., Callaghan et al. 2008b; Goddijn-Murphy et al. 2011) or planes (e.g., Bobak et al. 2011; Kleiss and Melville 2010). Typically, monochrome visible sensors are used, but whitecap coverage W has also been determined from multispectral visible (Randolph et al. 2017) and infrared (Jessup et al. 1997) imagery. Globally, W can be inferred from satelliteborne microwave radiometers (e.g., Anguelova and Webster 2006; Salisbury et al. 2013).

Being such a readily observable quantity, W has been recognized as a promising proxy for quantifying wave breaking-dependent processes that have complex impacts on the energy, momentum, heat, and mass transfer at the air-water interface. Large-scale wave breaking is the least understood key element in determining the

This is Lamont-Doherty Earth Observatory Contribution Number 8134.

Corresponding author: Sophia E. Brumer, sbrumer@ldeo.columbia.edu

DOI: 10.1175/JPO-D-17-0005.1

© 2017 American Meteorological Society. For information regarding reuse of this content and general copyright information, consult the AMS Copyright Policy (www.ametsoc.org/PUBSReuseLicenses).

evolution of wave fields and needs to be properly represented in wave models. It generates turbulent kinetic energy in the upper ocean, drives near-surface mixing, and transfers energy from the wave system to surface currents and longer waves (Cavaleri et al. 2007). Breaking waves and their consequent whitecaps play a significant role in the climate system (Cavaleri et al. 2012). They directly influence the ocean surface albedo and hence the surface radiation budget. It has been estimated that they contribute to a globally averaged cooling of about 0.03 W m^{-2} (Frouin et al. 2001). Because of their impact on albedo, whitecaps must be accounted for in remote sensing applications such as retrieval of surface wind (Gaiser et al. 2004) and ocean color (Gordon and Wang 1994).

Many studies have also shown that, through additional turbulence and bubble mediated transfer, wave breaking leads to enhanced air–sea transfer of gases (Wallace and Wirick 1992; Farmer et al. 1993; Asher et al. 1995; Asher and Wanninkhof 1998; Monahan and Spillane 1984; Woolf 1997; Woolf et al. 2007). These experiments led to several whitecap-dependent gas transfer parameterizations. Furthermore, bursting of the bubbles at the surface injects sea spray aerosols into the atmosphere, and the aerosol production flux is thought to be directly proportional to the whitecap coverage (de Leeuw et al. 2011, and references therein). These sea salt aerosols play an important role in Earth’s radiation budget. They are cloud condensation nuclei, influencing the microphysical and radiative properties of clouds. They are also direct scatterers of solar radiation (Andreae and Rosenfeld 2008; Haywood et al. 1999).

The W has traditionally been parameterized as a nonlinear function, most commonly a power law, of the 10-m wind speed U_{10} , which is easily and routinely measured and modeled. The first empirical function suggested was a simple two coefficient power law (Monahan 1971):

$$W(U_{10}) = aU_{10}^n. \quad (1)$$

Later, a new functional form was proposed that accounts for a minimum wind speed threshold, below which no whitecaps are observed (Monahan 1993; Asher and Wanninkhof 1998), and forced a cubic dependence on wind speed ($n = 3$):

$$W(U_{10}) = a(U_{10} - b)^n. \quad (2)$$

The cubic wind speed dependence was adopted based on the hypothesis that W is strongly related to the energy flux from the wind, which scales as u_*^3 (Phillips 1985; Wu 1988), where u_* is the airside friction velocity. However, a cubic dependence on wind speed is questionable, and there is no reason not to allow for a tunable exponent. Indeed, satellite-derived W displays a dependence on wind speed closer to quadratic (Salisbury et al. 2013),

while most recent nonthresholded power-law fits suggest an exponent greater than 3 (Table A1).

Anguelova and Webster (2006) compiled parameterizations of W as a function of U_{10} found in the literature prior to 2005. The wind speed–only parameterizations published since then are tabulated in Table A1 and plotted in Fig. 1. While the historical parameterizations, summarized in Anguelova and Webster (2006), exhibit several orders of magnitude scatter, recent parameterizations can be seen to agree more closely between studies. A variety of different detection techniques used in the past could explain the majority of the scatter between previous studies. Recent advances in instrumentation, and the adoption of an automated and objective image processing algorithm (Callaghan and White 2009), have resulted in more consistent whitecap detection. It is also important to note that parameterizations are typically used over a wind speed range that goes beyond the range from which any given parameterization was determined, which may lead to significant errors. Individual projects sample only a limited set of environmental conditions and exhibit large scatter. This leads to different trends as determined from best fits and parameterizations that diverge from one study to the next. This divergence is exacerbated at the low and high wind speed tails, and extrapolating parameterizations beyond their valid range results in increased apparent scatter. However, at least from recent data, at a given wind speed, scatter is comparable from one study to the next, and the mean W do not differ significantly (see de Leeuw et al. 2011, their Fig. 2).

Remaining scatter suggests that wind speed alone does not account for all the observed W variability. Indeed, a multitude of factors have been recognized to affect wave breaking and bubble lifetime and thereby influencing whitecap coverage (Melville 1996; Salisbury et al. 2013). These include surfactants (Frew 1997), salinity, sea surface temperature (Spillane et al. 1986), atmospheric stability (Myrhaug and Holmedal 2008; Spillane et al. 1986), wind fetch and duration (Myrhaug and Holmedal 2008), current shear, and long-wave interaction (Kraan et al. 1996). The effects of these factors are more often than not studied separately. The typical approach is to group observations into several ranges of similar conditions based on one factor and compute different coefficients to the wind speed power laws for each range. Salisbury et al. (2013) looked at the variability in W after removing the dominant wind speed dependence and showed that the most important secondary factor is the wave state.

Since the scatter displayed by wind speed–only parameterizations is thought to be largely due to varying wave conditions, parameterizations have emerged in the recent literature that account for both wind speed and sea state. These are summarized in Tables A2 and A3.

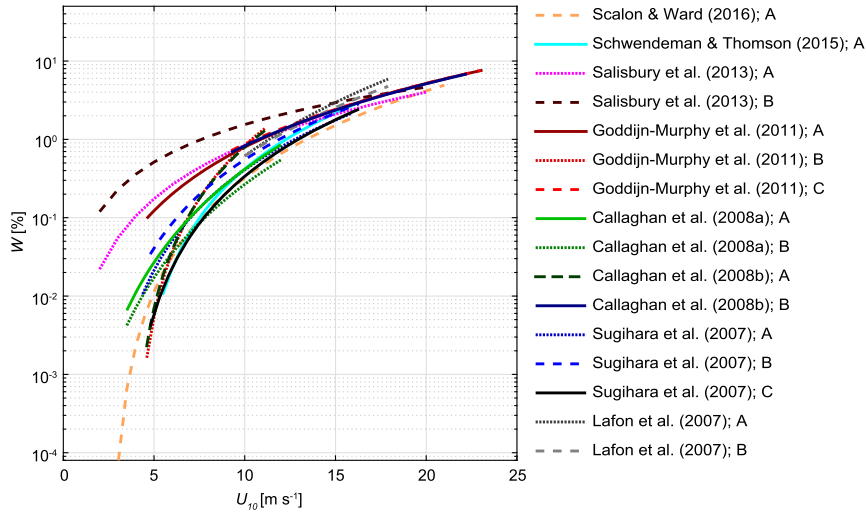


FIG. 1. Parameterizations of whitecap coverage W as a function of wind speed U_{10} published since 2004 (see Table A1).

Zhao and Toba (2001) suggested that W is better constrained as a function of wind-sea Reynolds numbers than wind speed alone. The breaking wave Reynolds number was first proposed by Toba and Koga (1986) and is defined as

$$R_B = \frac{u_*^2}{\nu_w \omega_p}, \quad (3)$$

where ν_w is the kinematic viscosity of water, and ω_p is the peak angular frequency of wind waves. Zhao and Toba (2001) introduced an alternative Reynolds number:

$$R_{H_a} = u_* H_s / \nu_a, \quad (4)$$

where H_s is the significant wave height, and ν_a is the kinematic viscosity of air. Both Zhao and Toba (2001) and Woolf (2005) suggested that it is more appropriate to use ν_w rather than ν_a to characterize wave breaking in the open ocean and suggested

$$R_{H_w} = u_* H_s / \nu_w. \quad (5)$$

Although these Reynolds numbers were originally defined for wind seas, subsequent studies computed them with wave statistics from the full spectrum, which may contain both swells and wind sea (Norris et al. 2013; Goddijn-Murphy et al. 2011). While R_{H_w} was termed the wave roughness Reynolds number in Norris et al. (2013), it will hereinafter be referred to as the wind-wave Reynolds number to highlight that it incorporates both a wind and wave dependence. Note that the Reynolds numbers may also be able to account for the dependence on temperature and salinity as these dictate the kinematic viscosity (Nayar et al. 2016; Sharqawy et al. 2010).

The whitecap coverage has also been shown to depend on wave age (c_p/u_* , where c_p is the phase speed at spectral peak), with decreased W observed in old, swell-dominated seas compared to young, wind-wave seas (e.g., Schwendeman and Thomson 2015b). For transitional and shallow-water waves, an inverse dependence of whitecap coverage on wave age has been observed (Sugihara et al. 2007). Based on the relation of W to the wave breaking-induced energy dissipation, as proposed by Komen et al. (1994), Kraan et al. (1996) deduced a relation between W and the integral wave steepness [$\bar{\alpha} = \bar{\omega}^4 g^{-2} \int E(\omega) d\omega$, where $\bar{\omega}$ is the mean angular frequency and E is the omnidirectional wave spectrum]: $W = 24\bar{\alpha}^2$. Expressing $\bar{\alpha}$ as a function of wave age, they deduced a wave age-dependent parameterization of W . Multiple later studies (Callaghan et al. 2008b; Guan et al. 2007; Lafon et al. 2007, 2004; Schwendeman and Thomson 2015b) have determined additional power-law parameterizations of whitecap coverage as functions of wave age. These are tabulated in Table A3. Note that Schwendeman and Thomson (2015b) gave coefficients for the inverse wave age, and the parameterizations reported in Table A3 were computed by fitting a power law to their parameterization.

Fewer studies suggested parameterizations of W as a function of the turbulent kinetic energy dissipation ε . This is because only a few studies have been undertaken in which both of the near-surface ε and whitecap coverage were measured (Schwendeman and Thomson 2015b). Such parameterizations will not be addressed in this paper.

The idea that wave breaking occurs once a critical local steepness is reached dates back over a century (Stokes 1880) and is at the core of many probability models of wind-wave breaking. However, few studies have related W

to steepness since [Kraan et al. \(1996\)](#). While local steepness is difficult to measure, average wave steepness parameters are easy to compute from 1D wave spectra based on a characteristic wave height H and wavenumber k :

$$S = \frac{Hk}{2}. \quad (6)$$

Typically, either the peak or mean wavenumbers are considered, and the peak, mean, or significant wave heights are used to compute S ([Kleiss and Melville 2010](#); [Schwendeman and Thomson 2015b](#)). However, whitecaps are typically associated with steeper and shorter waves than the dominant or mean wave system, which often corresponds to swell. It has therefore been argued that a measure of the mean square slope (mss) as suggested by [Banner et al. \(2002\)](#) is a more appropriate measure. The mss is calculated as

$$\text{mss} = \int \frac{(2\pi f)^4 E(f)}{g^2} df, \quad (7)$$

where $E(f)$ is the omnidirectional wave spectral energy density. The frequency range over which the mss is evaluated is typically chosen as the equilibrium range spanning $\sqrt{2}f_m \leq f \leq \sqrt{5}f_m$ ([Schwendeman and Thomson 2015b](#)), where f_m is the mean frequency computed as

$$f_m = \frac{\int fE(f)df}{\int E(f)df}. \quad (8)$$

[Schwendeman and Thomson \(2015b\)](#) found the mss most promising for improving W parameterization, especially when normalized by directional spread $\Delta\theta$ ([Kuik et al. 1988](#)) and frequency bandwidth Δf .

Few parameterizations other than wind speed only have been rigorously tested beyond the original studies and not many datasets exist with concurrent W and wavefield measurements. The synergy of measurements taken during the Southern Ocean (SO) Gas Exchange Experiment (GasEx) and the recent High Wind Speed Gas Exchange Study (HiWinGS) offer unique datasets that facilitate testing of new and existing W parameterizations. In this paper, the dependence of whitecap coverage on wind speed and sea-state conditions is investigated with the aim of improving whitecap parameterizations to be used in gas transfer and climate models. The SO GasEx and HiWinGS field campaigns are described in [section 2](#) along with details of supporting measurements and of the WAVEWATCH III (WW3) hindcast used to complement in situ wave observations. After a brief explanation of the image processing and wavefield analysis methods

in [section 3](#), the results are presented in [section 4](#) and discussed in [section 5](#). [Section 6](#) summarizes key findings and provides recommendations for whitecap parameterizations and future studies.

2. Data

a. The SO GasEx cruise

The SO GasEx cruise was the third and most recent cruise of the U.S.-led GasEx series initiated in 1998. The main GasEx objective was to improve quantification of air–sea CO_2 fluxes and gas transfer velocities. The aim of this third cruise was to examine these processes at higher wind speeds and obtain data in a previously unexplored region. The SO GasEx project focused on a study area around 51°S , 36°W , where the R/V *Ronald H. Brown* remained for 37 days, having left Punta Arenas, Chile, on 28 February 2008 ([Fig. 2a](#)). It is important to note that the ship was rarely stationary, as deliberate tracer release surveys were conducted on site. The study location was chosen for its high wind speeds and large air–water pCO_2 difference. The average 10-m neutral wind speed U_{10N} measured in the main study location was $9.7 \pm 3.2 \text{ m s}^{-1}$, and a maximum wind speed of 20.7 m s^{-1} was recorded during transit back to Uruguay, where the cruise ended on 9 April 2008 ([Fig. 3a](#)). To avoid a storm between 13 and 17 March, the R/V *Ronald H. Brown* moved temporarily into the lee of South Georgia Island. Water temperatures in the study site varied between 5° and 7°C , increasing to 14°C in the transit legs. For further details about SO GasEx, see [Ho et al. \(2011\)](#), [Edson et al. \(2011\)](#), and [Cifuentes-Lorenzen et al. \(2013\)](#).

b. The HiWinGS cruise

With the aim of gaining new insights into poorly understood aspects of air–sea interaction under high winds, the HiWinGS cruise objective was to deploy direct measurements of trace gas and physical fluxes together with a suite of wave physics and sea-state observations. The HiWinGS cruise took place on board the R/V *Knorr*, in the North Atlantic ([Fig. 2b](#)), departing Nuuk, Greenland, on 9 October 2013 and ending at Woods Hole, Massachusetts, on 14 November 2013. The ship's track was chosen based on daily analysis of weather maps and forecasts from the European Centre for Medium-Range Weather Forecast model provided by the Icelandic Met Office as well as from [PassageWeather.com](#) with the aim of maximizing the amount of time spent in the strongest winds. Along the track, the ship stopped at several stations for buoy deployments. While on station, the ship was positioned bow pointing into the wind for the duration of each storm.

The ship remained in the Labrador Sea, south of Greenland, for the first ~ 20 days of the cruise. Sea

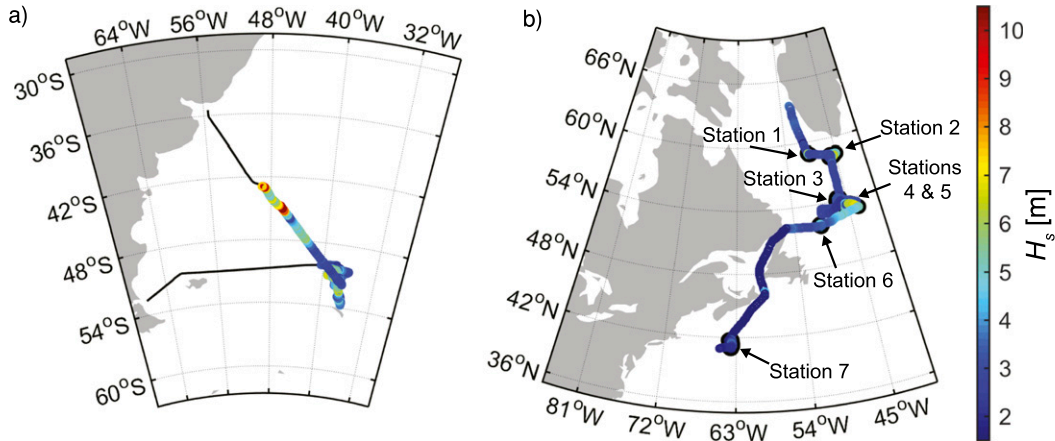


FIG. 2. Ships tracks (a) SO GasEx and (b) HiWinGS; the color code shows the significant wave height (m).

surface temperature and salinity were around 6°–8°C and 34–34.5 psu, respectively, at the first six stations (Fig. 2b). The ship then transitioned through the Gulf of St. Lawrence from 4 to 6 November 2013, and the last station was south of Nova Scotia where warmer and higher-salinity Gulf Stream waters were encountered with SST of 20°C and salinity of 36 psu. Wind speeds exceeded 15 ms⁻¹ 25% of the time amounting to a total of 189 h of wind speeds above 15 ms⁻¹, of which 48 h had wind speeds greater than 20 ms⁻¹. On 25 October 2013 (station 4), wind speeds exceeded 25 ms⁻¹ with gusts of 35 ms⁻¹ in the early stages of what became known as the St. Jude’s day storm (Fig. 3b).

c. Visible imagery

During SO GasEx, a total of 216 20-min video segments were recorded, while during the HiWinGS cruise, over 500 20-min segments were recorded, of which 50 were taken during the St. Jude’s day storm. For both experiments, the

imaging system consisted of two obliquely angled Imperx model Lynx 1M48 digital video cameras, with a sensing array of 1000 × 1000 elements of 7.4 μm. These were mounted on the flying bridge of the R/V *Knorr* and R/V *Brown* at a height above the water line of 14.7 and 25 m, respectively. For both experiments, one of the cameras was directed starboard, while the other one was mounted on the port side to accommodate all lighting conditions. During HiWinGS, wide field-of-view (FOV) lenses (68.7° FOV; 6-mm focal length) were used, whereas during SO GasEx lenses with 9-mm focal length and a FOV of 36.6° were used. The visible cameras ran at a frame rate of 20 Hz during HiWinGS and 5 Hz during SO GasEx.

The imaging system was improved for HiWinGS by the addition of inertial motion units (IMU) mounted on the same metal plate as the cameras to record the pitch, roll, and yaw angles of the cameras. An Xsens model MTi IMU was mounted on the port side system, while a 3DM-GX2 model MicroStrain IMU was affixed to the starboard

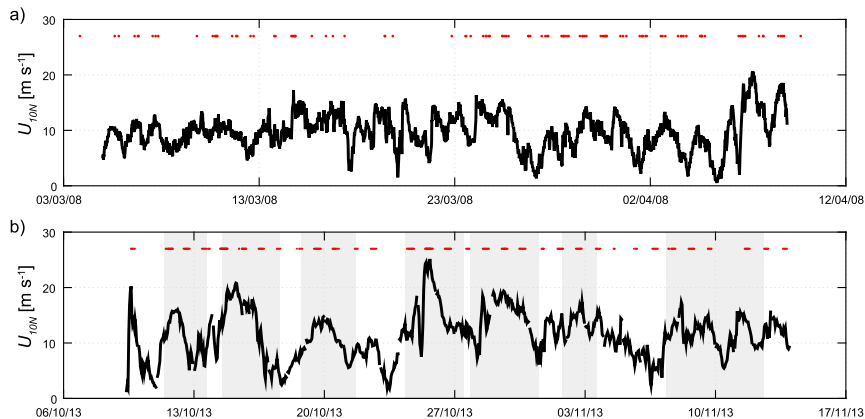


FIG. 3. Wind speed time series (a) for SO GasEx and (b) for HiWinGS. The gray shading represents periods when the ship was on station during HiWinGS. The red lines correspond to periods of visible imagery recording.

camera mount. The Xsens, which has an angular resolution of 0.05° , recorded at ~ 100 Hz, while the MicroStrain, which has an angular resolution of $<0.1^\circ$, recorded at 50 Hz. Both sensors have a dynamic accuracy of $\pm 2.0^\circ$.

d. Meteorological measurements

Momentum, energy, and buoyancy fluxes were obtained via direct eddy covariance measurements during both SO GasEx and HiWinGS, along with mean measurements of wind speed, wind direction, air temperature, humidity, pressure, and downwelling solar and IR radiation. The University of Connecticut direct covariance flux system (Uconn DCFS; Edson et al. 1998; Edson et al. 2004) and the NOAA/ESRL/PSD system (Blomquist et al. 2006; Fairall et al. 2003) were deployed during SO GasEx. These were mounted on the jackstaff of the R/V *Brown* at a height of 18 m above the surface and consisted of three fast-response Gill R-3 sonic anemometers and five infrared gas analyzers (Li-Cor LI-7500) sampling at 20 Hz. Additionally, the systems included a GPS compass and Systron-Donner “MotionPak” used to correct for ship motion, as described by Edson et al. (1998). For a detailed description of the setup, the reader is referred to Edson et al. (2011).

The NOAA/ESRL/PSD wind motion system was also used during HiWinGS. It was mounted on the bow mast at 16 m above the water line with fast-response sensors set to sample at 10 Hz. Two additional sonic anemometers were deployed, a Gill model R2 from the University of Hawaii (UH) on the foremast at 15 m and a Gill Windmaster Pro from Plymouth Marine Laboratory on the main mast, some distance behind the bow. While the measurements are mostly consistent between systems, only the measurements from the UH sonic and the MotionPak are considered here, as the NOAA system suffered a power outage during the St. Jude storm that put several instruments out of action. Direct eddy covariance fluxes and bulk fluxes from the COARE3.5 algorithm (Edson et al. 2013; Fairall et al. 2003, 2011) were computed over 15-min intervals for SO GasEx and hourly for HiWinGS.

e. 1D and directional wave spectra

1) IN SITU AND REMOTELY SENSED MEASUREMENTS

Directional ocean wave spectra were obtained with a Wave and Surface Current Monitoring System (WaMoS II) during SO GasEx (Cifuentes-Lorenzen et al. 2013; Lund et al. 2017). These measurements are based on the radar backscatter of sea clutter in which the wave patterns are distinguishable. The system used the unfiltered output from a marine X-band radar mounted on the flying bridge of the R/V *Brown* operating at 9.41 GHz to

determine wave and surface current parameters. The WaMoS II has the capability to resolve two-dimensional maps of the surface elevation and allowed for continuous day and night real-time measurements even in rough seas and harsh weather conditions. WaMoS II provides directional wave spectra and individual wave state components at scales of $O(100)$ m.

During HiWinGS, a Datawell DWR-4G Waverider buoy of 0.4-m diameter was deployed while on station for the duration of each major storm system. The Waverider uses the Doppler shift of the GPS signal carrier wave to obtain a direct measurement of its velocity in three dimensions at 1.28 Hz. These are integrated to obtain a time series of the three-dimensional displacement, from which directional wave spectra can be derived. The spectral frequency range resolved by the Waverider covers 0.025 to 0.6 Hz, corresponding to waves of wavelength greater than 4.3 m. During most deployments, the Waverider was left to drift freely within 5 km of the ship. The Waverider was tethered to the ship with a 200-m polypropylene line during the first deployment because of operational restrictions and during the largest storm (station 4) because of severe wind and wave conditions that would not have allowed the ship to stay within radio contact of the buoy. While the tether remained slack and the buoy was kept outside of the ship's wake on the first deployment, it regularly dragged the buoy under water during the peak wind period on station 4. This led to loss of GPS reception and poor data quality during part of the St. Jude storm. These data were discarded from subsequent analysis.

In addition, short to moderate gravity waves were measured using a Riegl laser altimeter (model LD90-3100VHS) during both experiments. The laser operates at a wavelength of $0.9 \mu\text{m}$ (near infrared), with a beam divergence of 2.7 mrad that corresponds to a footprint on the ocean surface of 2.65 cm at a range of 10 m. The manufacturer-specified measurement accuracy is $O(2.0)$ cm with a precision of $O(0.25)$ cm. The LD-90 laser altimeter data independently characterized spatial and temporal properties of the wave height field resolved down to $O(20)$ cm wavelengths (Zappa et al. 2012).

The Riegl was mounted on the jackstaff of the R/V *Knorr* at about 14.4 m during HiWinGS and on the jackstaff of the R/V *Brown* at 10 m above the mean water level during SO GasEx. Internal processing provided range to surface measurements at 10 Hz, which were corrected for the ship's heave following Cifuentes-Lorenzen et al. (2013) to provide the wave surface displacement. Midway through HiWinGS, after the St. Jude storm on 25 October 2013 at station 4 (see Figs. 2b and 3b), the Riegl stopped functioning because of a power distribution failure.

2) WAVEWATCH III HINDCAST

As flux measurements were taken continuously during the HiWinGS cruise and visible imagery was taken regularly during daylight periods regardless of whether the ship was steaming or on station, the in situ wave data were complemented by a model hindcast. Version 3.14 of WW3 (Tolman 2009) was used to compute the hindcast for the duration of the cruise from 1 October to 15 November 2013 (2.5 months). The model domain was set to cover the North Atlantic (0° – 70° N, 100° W– 15° E) with a latitudinal and longitudinal grid resolution of 0.2° . Bottom topography and coastlines were taken from the ETOPO2 dataset that provides 2-min gridded elevations/bathymetry for the world. The wave model was forced by 6-hourly surface wind fields from the National Centers for Environmental Prediction (NCEP)/Climate Forecast System Reanalysis (CFSR) product (Saha et al. 2010), which has a horizontal resolution of ~ 38 km (Gaussian grid: T382).

WW3 solves the wave spectral balance equation, which dictates the evolution of the wave field based on the sum of source terms consisting of the energy transferred to the waves by the wind S_{in} , the energy lost through dissipation due to wave breaking S_{dis} , and nonlinear wave–wave energy transfers S_{nl} :

$$\frac{DN}{Dt} = \frac{S_{\Sigma}}{\sigma} = (S_{\text{in}} + S_{\text{nl}} + S_{\text{dis}})/\sigma, \quad (9)$$

where $N = N(t, x, y, f, \theta)$ is the wave action density spectrum, S_{Σ} is the sum of source terms, and σ is the intrinsic (radian) frequency. The term DN/Dt denotes the total time derivative: $DN/Dt = \partial N/\partial t + \nabla_x[(\mathbf{c}_x + \mathbf{u})N] + \nabla_i(\mathbf{c}_i N)$, where \mathbf{u} is the current; \mathbf{c}_x is the propagation, that is, group velocities in geographical space (x, y); and \mathbf{c}_i is the propagation velocities in spectral space (f, θ).

For the HiWinGS hindcast, the source terms proposed by Tolman and Chalikov (1996) were used and the surface wind speed at 10-m elevation was modified to account for the instability of the atmospheric boundary layer (the effective wind speed; Tolman et al. 2002). Being a third-generation model, WW3 allows for a punctual, although approximate, representation of S_{nl} , for which the discrete interaction approximation (DIA) method was chosen (Hasselmann et al. 1985). For spatial propagation of the wave spectrum, the default third-order advection scheme was used.

The spectral space was discretized using 35 frequencies ranging from 0.04 to 1.05 Hz in 10% steps ($f_{i+1} = 1.1f_i$, where i is a discrete grid counter) with 36 directions ($\Delta\theta = 10^{\circ}$). An f^{-5} spectral tail outside the model frequency range was assumed, as per default WW3 settings. The directional wave spectra from the hindcast were

stored every 30 min along four trajectories following the ship's track.

3. Methods

a. Image analysis

Initial visual quality control led to removal of video segments that were affected by sun glare or taken in otherwise poor light conditions. Segments were also removed based on the presence of birds that tend to be falsely identified as whitecaps. The first step of the image analysis was to crop the images in order to avoid the ship's wake when the ship was steaming and to remove the horizon from the field of view. An example of images taken while on station during HiWinGS is shown in Fig. 4a. Before applying the typical brightness threshold (Callaghan and White 2009) to the images, all background gradients were removed. This was achieved in a two-step process: the images are prethresholded to identify any pixel with brightness greater than 3.25 standard deviations above the mean; then the row and column means are computed, ignoring the high brightness pixels, and these means were subtracted from each pixel. Prethresholding avoids brightness bleeding when removing background gradients.

Removing background gradients was found to greatly improve subsequent whitecap detection via the typical automated brightness threshold techniques. A test dataset was used to evaluate the effectiveness of flattening the background intensity gradient for removing biases arising from varying brightness and exposure settings. This dataset consisted of imagery taken over the course of 2 days during HiWinGS from two Mobotix MX-M24M IP cameras with 32-mm lenses, providing a 60° field of view, on the starboard side of the R/V *Knorr* with closely matched fields of view. One camera setting remained unchanged during the test while the target brightness and exposure settings were changed on the other one. Ignoring the background gradients resulted in up to a factor of 4 difference between W determined from the two cameras; removing them reduced the difference to a factor of 0.7 to 1.04.

Whitecaps were then isolated in the preprocessed rectified images by the automated whitecap extraction (AWE) algorithm (Callaghan and White 2009), which computes the most suitable brightness threshold for each individual image based on the derivatives of an image structure function. The AWE algorithm has been used successfully to analyze large datasets (Callaghan et al. 2008a,b; Goddijn-Murphy et al. 2011; Scanlon and Ward 2013, 2016; Schwendeman and Thomson 2015b; Schwendeman et al. 2014) and has been shown to provide robust W results.

The thresholded images are orthorectified to compute W . This is achieved by first correcting for lens distortion

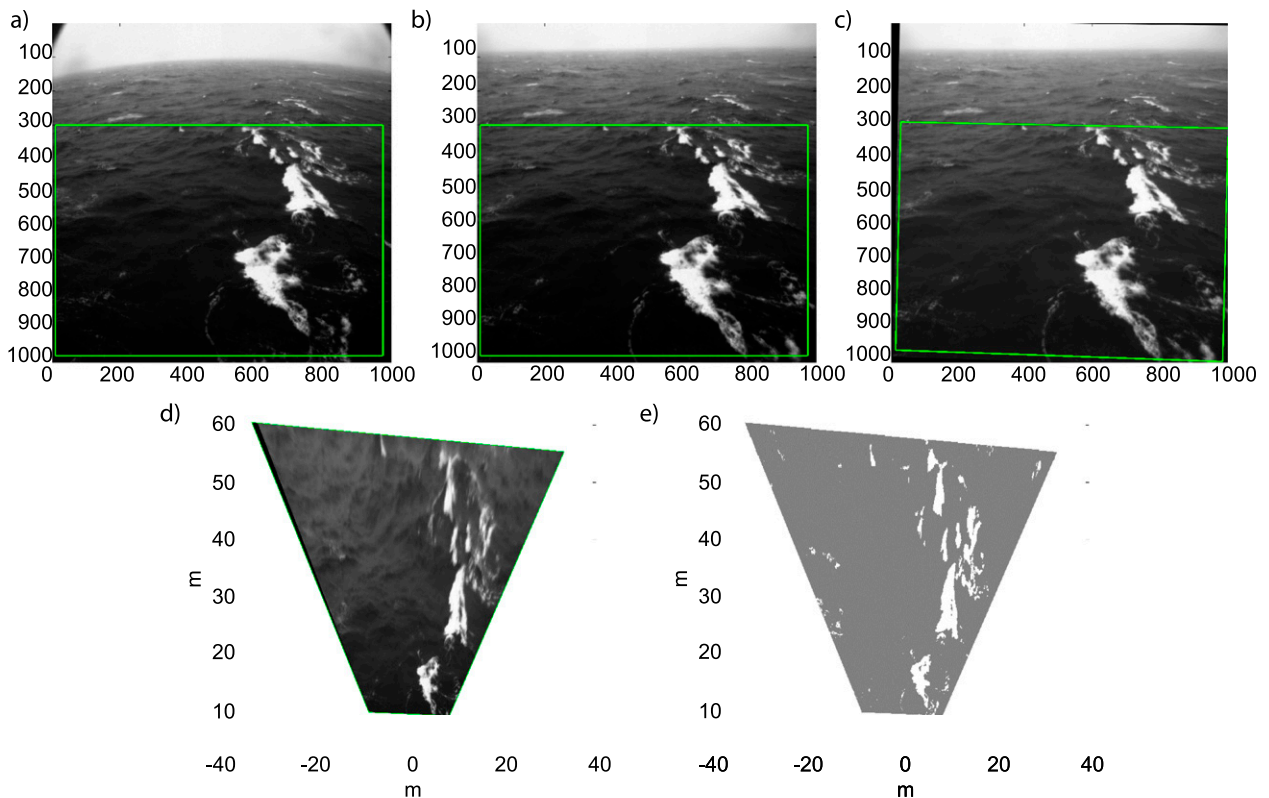


FIG. 4. Steps of the image processing: (a) raw image, (b) lens calibration, (c) roll and yaw correction, (d) projection based on incidence angle and height of camera assuming flat surface, and (e) thresholded and projected image.

based on intrinsic parameters determined using the camera calibration toolbox for MATLAB (Bouquet 2015). The effect of the lens distortion can clearly be seen in the noncropped raw imagery in Fig. 4a and its correction in Fig. 4b. Then, georectification is performed by applying the 3D rotation matrix based on the roll, pitch, and yaw angles (Holland et al. 1997; Schwendeman and Thomson 2015a). This step is illustrated in the raw imagery in Figs. 4c and 4d. Finally, the thresholded images are interpolated onto the regular, georectified grid with pixel dimensions of 0.01 m^2 (Fig. 4e), W is determined for each image, and an average W is computed for each 20-min segment.

At this point, an additional quality control step was undertaken, and cumulative whitecap coverage W_{CA} was computed based on the whitecap coverage W_{frame} determined from a single frame F , normalized by the 20-min-averaged whitecap coverage $W_{20\text{min}}$:

$$W_{CA_{\text{norm}}}(F) = \frac{W_{CA}(F)}{W_{20\text{min}}} = \left[\sum_{i=1}^F \frac{W_{\text{frame}}(i)}{F} \right] / W_{20\text{min}}.$$

Time series of $W_{CA_{\text{norm}}}$ show that for the most part $W_{CA_{\text{norm}}}$ converges quickly toward unity staying within one standard deviation bounds ± 0.3 and ± 0.17 after 10 and

15 min, respectively (Fig. 5). Several video segments, however, do not appear to converge within 20 min. Non-converging $W_{CA_{\text{norm}}}$ were identified based on standard deviation bounds computed from $W_{CA_{\text{norm}}}$ of the entire dataset for a given time (or frame number). Data were flagged if it fell outside the two standard deviation bound after 15 min and were excluded from subsequent analysis. There does not seem to be a clear dependence of the convergence time on wind speed or wave age, which could require a wind- and sea-state-dependent averaging time scale. Note that an alternative approach to evaluate convergence of W can be found in Callaghan et al. (2008a).

After removing these data, the 20-min W estimates were averaged to give hourly estimates on the same time intervals as the fluxes yielding 97 and 176 hourly means for SO GasEx and HiWinGS, respectively. Note that when comparing W to wave statistics, the number of hourly concurrent data points is 73 for SO GasEx and 172 for HiWinGS, which is further reduced to 34 and 138 when considering wind seas for SO GasEx and HiWinGS, respectively.

While an IMU was mounted in each camera housing during the HiWinGS campaign recording the rotation angles that allow for projection and scaling of the images, this was not the case during SO GasEx. Instead,

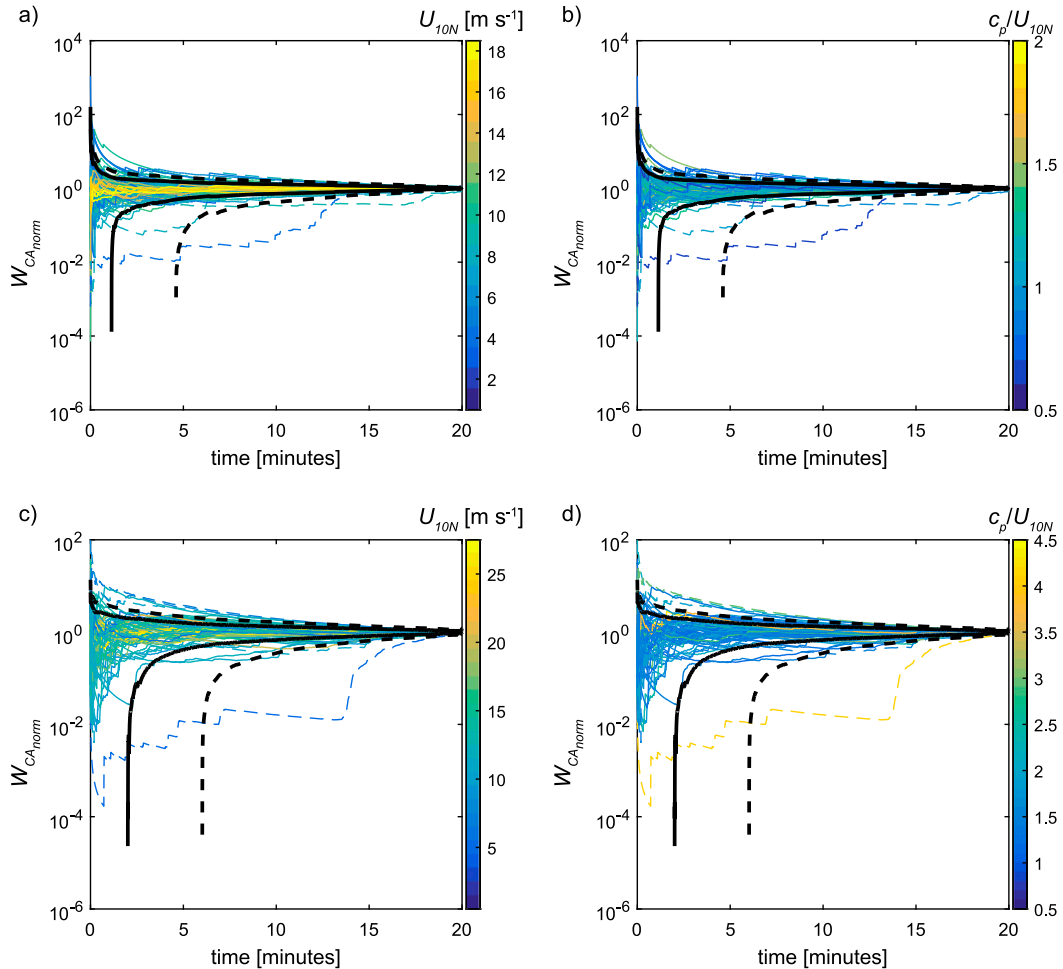


FIG. 5. Time series of the normalized cumulative whiteness coverage $W_{CA_{norm}}$ color coded by (left) wind speed and (right) wave age for (a),(b) SO GasEx and (c),(d) HiWinGS. The black solid and dashed lines represent the one and two std dev bounds computed from $W_{CA_{norm}}$ of the respective datasets for a given time. Nonconverging $W_{CA_{norm}}$ are represented by lines that fall outside of the two std dev bound after 15 min for more than 3 min.

rotation angles were determined by tracking the horizon (Schwendeman and Thomson 2015a). To test the performance of the horizon tracking algorithm, it was applied to the HiWinGS imagery, and the computed angles were plotted against those computed from the IMUs. As shown in Fig. 6, the horizon tracking algorithm is successful at retrieving the roll and pitch angles. However, it generates erroneous attitude angles easily detectable as spikes in the pitch and roll time series. Depending on the type of analysis to be subsequently performed on the imagery, individual frames may be discarded or despiking algorithms (e.g., Mori et al. 2007) may be applied.

b. Wavefield statistics

Wavefield statistics were determined both from the directional spectra given by the Waverider, the WAMOS, and the WW3 hindcast and the 1D spectra obtained from

the Riegl. The raw 3D displacement measurements of the Waverider were used to compute hourly spectra using the DIWASP toolbox (Johnson 2012) to match the time scale of the other data. Half hourly wave spectra obtained from the four WW3 hindcast tracks were averaged to get hourly spectra. Figure 7 shows the spectrogram and an example of a directional spectrum from the WAMOS; those from the Waverider and WW3 are shown in Fig. 8.

Wave statistics were first computed from 1D spectra measured by the Riegl or from the directionally integrated spectra of the WAMOS, Waverider, and WW3 using a standard processing method. Similarly, a standard protocol was applied to the directional spectra to separate wind seas and swell and to get wave statistics for individual wave groups (Hanson and Phillips 2001). The computed wave statistics include the peak f_p and mean f_m frequencies, the

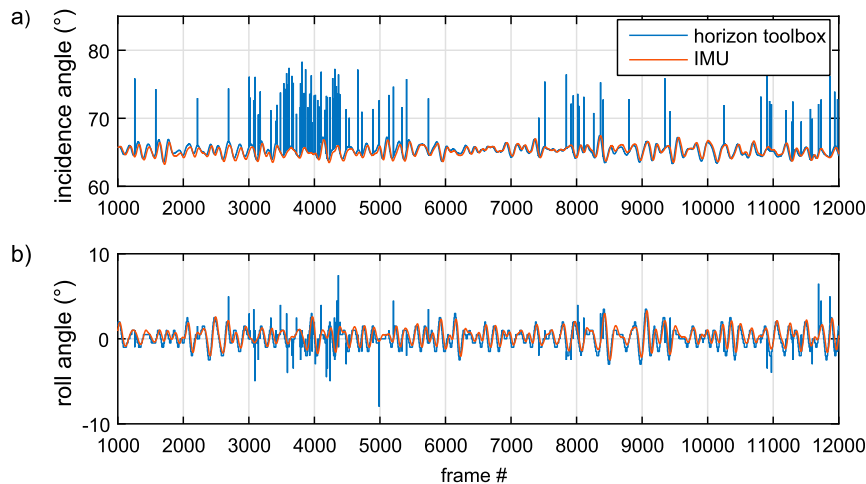


FIG. 6. time series of the (a) incidence and (b) roll angles measured by the IMU (orange) and determined by the horizon tracking toolbox (blue).

peak and mean phase velocities (c_p and c_m , respectively), as well as the significant $H_s = 4 \left[\int E(f) df \right]^{1/2}$, peak $H_p = 4 \left[\int_{0.7f_p}^{1.3f_p} E(f) df \right]^{1/2}$, and mean $H_m = 4 \left[\int_{0.7f_m}^{1.3f_m} E(f) df \right]^{1/2}$ wave height of the entire wave field or individual wave system. When computing statistics for individual systems, we distinguish between wind sea and swells, merging systems so as to have at the most a single wind sea and a single swell system.

No comparison of the statistics obtained from the different datasets is discussed here. Intercomparison of various wave measurements and validation of the WW3 hindcast for HiWinGS will be reported in a separate paper along with a detailed description of the analysis methods applied to the directional spectra. An intercomparison between the Riegl and WAMOS data recorded during SO GasEx can be found in Cifuentes-Lorenzen et al. (2013), while Lund et al. (2017) show a comparison of wind-sea and swell statistics obtained from WAMOS and WW3 for SO GasEx. As the statistics obtained from the various datasets are consistent for each experiment, results are reported based on WAMOS and WW3 statistics to allow usage of the full range of whitecap data.

c. Determination and evaluation of parameterizations

Wind- and wave-dependent parameterizations are determined through weighted least squares fits of binned data for each dataset individually and combined. The binning was done using the equidensity method with each bin containing seven data points, rather than at regular intervals of wind and/or wave statistics. The reciprocal of the standard error in each

bin was used as weights. Two fit statistics are reported to help evaluate the parameterizations: 1) the root-mean-square error $\text{rmse} = \sqrt{\sum (W_{\text{obs}} - W_{\text{param}})^2 / N}$, where W_{obs} are the hourly estimates of W , W_{param} are the W obtained from the parameterizations, and N the number of estimates; and 2) the correlation coefficients $r^2 = 1 - \frac{\sum (\log_{10} W_{\text{obs}} - \log_{10} W_{\text{param}})^2}{\sum (\log_{10} W_{\text{obs}} - \log_{10} W_{\text{obs}})^2}$, where the overbar represents the dataset average, computed as in Schwendeman and Thomson (2015b) based on the log residual so as to equally weight data points across orders of magnitude. Note that all fits were performed in linear space and both W and the root-mean-square errors (rmse) are reported in %. Note also that no consistent way of computing the rmse has been used in the literature and that these therefore are not directly comparable to previous studies such as Schwendeman and Thomson (2015b) and Goddijn-Murphy et al. (2011).

4. Results

a. Whitecap dependence on wind speed alone

Following the traditional approach, the dependence of W on wind speed alone is assessed. As seen in Fig. 9a, the So GasEx and HiWinGS data fall within the recent wind speed-only parameterizations reported in the literature since 2004.

Results of the weighted least squares fit for a thresholded power law [(2)] are listed in Table 1 along with the appropriate fit statistics. The power-law fits to the individual and combined datasets agree closely with exponents closer to 1 than 3. It appears that the whitecap coverage saturates at high wind speeds

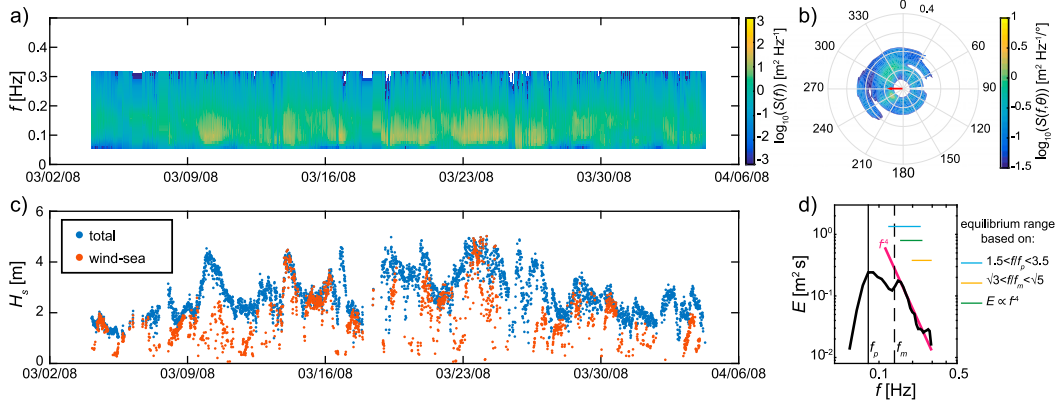


FIG. 7. WAMOS measurements taken during SO GasEx: (a) the spectrogram, (b) an example of a directional wave spectra, (c) the time series of the significant wave height computed from the total spectrum and the wind-sea partition, and (d) the omnidirectional wave spectra computed from (b) with vertical lines depicting the peak and mean frequencies and horizontal lines showing equilibrium ranges based on the peak frequency, the mean frequency, and portion of the spectra proportional to the frequency to the power -4 .

($U_{10N} > 22.5 \text{ ms}^{-1}$). The fit to the combined dataset most closely follows that suggested by Salisbury et al. (2013) based on the 10-GHz microwave satellite data. The rmse between the best fits determined here and the 10-GHz parameterization of Salisbury et al. (2013) is around 0.1%. The next closest parameterization is that of Goddijn-Murphy et al. (2011; A, Table A1) with an rmse to the best fit to the combined dataset of 1.4%. The rmse

between the best fits determined here and the other parameterizations plotted in Fig. 9a average around 2%.

Following the same approach as before, parameterizations of W as functions of the friction velocity were determined from the data. These are shown in Fig. 9b and listed in Table 1. Parameterizations from previous studies plotted here are summarized in Table A4. Based on the fit statistics, there does not seem to be an

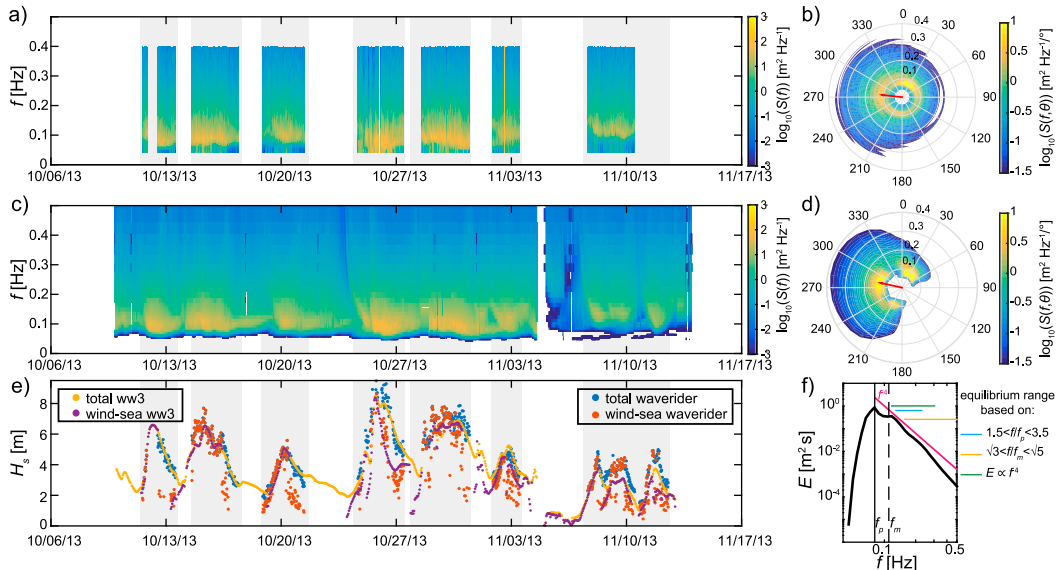


FIG. 8. Wavefield measurements and model hindcast for HiWinGS. (a),(c) Spectrograms from the Waverider and from the WAVEWATCH III hindcast, respectively. (b),(d) Examples of directional wave spectra from the Waverider and from the WAVEWATCH III hindcast corresponding to the same time. The time series of the significant wave heights computed from the total spectrum and the wind-sea partition of both the Waverider and the model hindcast is shown in (e), and (d) depicts the omnidirectional wave spectra computed from (d) with vertical lines depicting the peak and mean frequencies and horizontal lines showing equilibrium ranges based on the peak frequency, the mean frequency, and portion of the spectra proportional to the frequency to the power -4 . The gray shading in (a), (b), and (e) indicates periods when the R/V *Knorr* was on station.

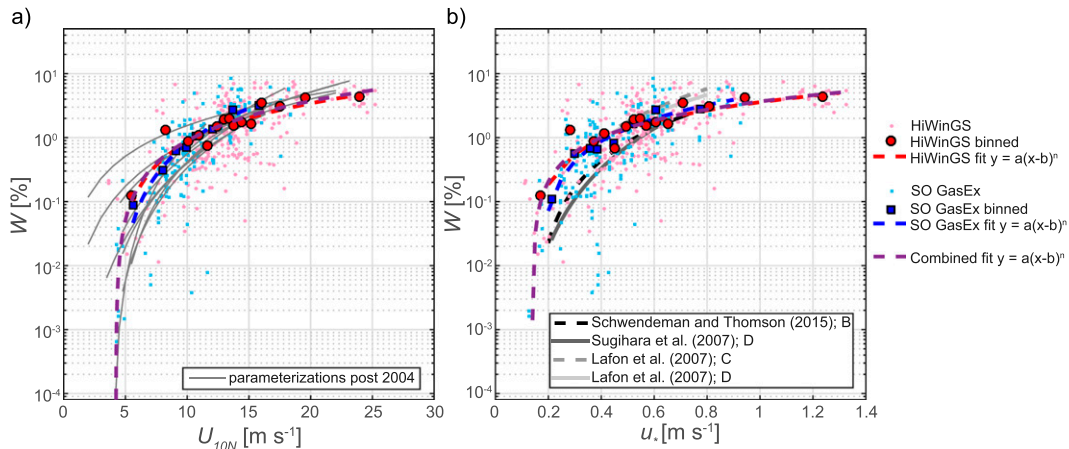


FIG. 9. Whitecap coverage W as a function of (a) the 10-m neutral wind speed U_{10N} and (b) the friction velocity u_* . The small light red dots show the hourly averaged whitecap coverage computed from the HiWinGS dataset, while the small blue squares are the 30-min-averaged whitecap coverage computed from the SO GasEx dataset. The blue squares and red circles show averages of seven neighboring points for SO GasEx and HiWinGS, respectively. These are used to compute the best fit shown by the dashed red and blue lines. The dark purple lines show the best fits to the binned combined data. The gray lines correspond to the parameterizations summarized in Tables A1 and A4.

improvement in using the friction velocity over the 10-m neutral wind speed. Again, the exponents of the thresholded power laws suggest a closer to linear than cubic relationship between W and u_* .

b. Whitecap dependence on sea state alone

In terms of pure sea-state parameterization, the relationship between W and various forms of wave steepness parameters S and mss were investigated. These statistics were computed from entire spectra as well as from the wind-sea-only partition. To compute S , three distinct wave heights (H_s , H_m , and H_p) were considered in combination with the two wavenumbers (k_p and k_m) computed via the linear deep-water dispersion relation $k = (2\pi f)^2/g$ from the peak and the mean frequency, respectively.

Simple power laws of the form $W(X) = aX^n$ were found to be more suitable than thresholded power laws for these statistics. The computed fits are listed in Table 2 along with the appropriate statistics. Based on the correlation coefficients r^2 , steepness and slope

parameters are poorer predictors for W than wind speed. Negative r^2 suggest that the model performs worse than a horizontal line. The rmse are also generally higher than for the wind-only fits. In general, very poor fits were obtained for SO GasEx. Of the wave steepness predictors, $(H_s k_m)/2$ gives the best fit for HiWinGS. Normalizing the mss by the directional spread and the frequency bandwidth yields only slightly improved fits. These two fits are shown in Fig. 10. They correspond to the steepness estimate and the normalized mss that were shown to best fit the northeast (NE) Pacific data published by Schwendeman and Thomson (2015b). While the HiWinGS data appear to fall along the best fit suggested by Schwendeman and Thomson (2015b) when plotted against the wave steepness $(H_s k_m)/2$, significantly higher W were observed over less steep waves during SO GasEx than by Schwendeman and Thomson regardless of the wave statistics used. Neither dataset shows much variation with mss whether normalized or

TABLE 1. Wind speed-only parameterizations of whitecap coverage determined in this study. Fits were computed from the binned averages, but statistics are reported with respect to the hourly estimates. Note that W is expressed as a percentage, as is its rmse. The correlation coefficients were computed in log space to give equal weight to the whitecap data across several orders of magnitude.

Experiment	Best-fit equation	Range (m s^{-1})	r^2	rmse
HiWinGS	$W = 8.07 \times 10^{-2} (U_{10N} - 4.45)^{1.37}$	$5.46 \leq U_{10N} \leq 23.96$	0.51	1.35
SO GasEx	$W = 2.31 \times 10^{-2} (U_{10N} - 4.20)^{2.03}$	$5.61 \leq U_{10N} \leq 15.82$	0.34	0.96
Combined	$W = 7.38 \times 10^{-2} (U_{10N} - 4.23)^{1.42}$	$4.56 \leq U_{10N} \leq 25.10$	0.48	1.22
HiWinGS	$W = 4.24 (u_* - 0.14)^{1.10}$	$0.17 \leq u_* \leq 1.24$	0.51	1.35
SO GasEx	$W = 5.84 (u_* - 0.17)^{1.30}$	$0.21 \leq u_* \leq 0.77$	0.16	1.00
Combined	$W = 4.32 (u_* - 0.14)^{1.09}$	$0.15 \leq u_* \leq 1.24$	0.37	1.24

TABLE 2. Wave steepness and mean square slope parameterizations of whitecap coverage (%) determined in this study. Wind-sea-only statistics are denoted by a ws subscript. Fits and data computed as for Table 1.

Predictor	Experiment	a	n	Range	r^2	rmse
mss	HiWinGS	1.47×10^4	1.63	1.43×10^{-3} – 5.32×10^{-3}	0.16	1.61
	SO GasEx	5.40×10^0	0.28	8.05×10^{-4} – 4.59×10^{-3}	–0.11	1.32
	Combined	1.72×10^2	0.82	6.48×10^{-4} – 5.35×10^{-3}	–0.04	1.56
mss _{ws}	HiWinGS	4.42×10^3	1.39	2.01×10^{-3} – 6.84×10^{-3}	–0.08	1.64
	SO GasEx	2.81×10^0	0.19	6.27×10^{-4} – 3.80×10^{-3}	–0.13	0.72
	Combined	1.73×10^3	1.22	3.87×10^{-4} – 6.16×10^{-3}	0.00	1.54
mss/ $\Delta\theta\Delta f$	HiWinGS	5.80×10^1	1.18	1.21×10^{-2} – 9.44×10^{-2}	0.28	1.49
	SO GasEx	5.96×10^0	0.52	1.34×10^{-2} – 7.71×10^{-2}	–0.19	1.33
	Combined	2.19×10^1	0.84	8.11×10^{-3} – 9.59×10^{-2}	0.02	1.49
mss _{ws} / $\Delta\theta\Delta f$	HiWinGS	5.95×10^1	1.17	1.65×10^{-2} – 1.16×10^{-1}	0.36	1.45
	SO GasEx	5.99×10^0	0.58	1.84×10^{-2} – 4.94×10^{-2}	–0.15	0.78
	Combined	4.99×10^1	1.09	1.10×10^{-2} – 9.55×10^{-2}	0.25	1.42
$H_s k_m/2$	HiWinGS	9.05×10^6	4.16	1.34×10^{-2} – 2.91×10^{-2}	0.21	1.54
	SO GasEx	1.91×10^2	1.23	1.03×10^{-2} – 2.06×10^{-2}	–0.19	1.30
	Combined	3.71×10^3	2.02	8.83×10^{-3} – 2.87×10^{-2}	0.05	1.48
$H_m k_m/2$	HiWinGS	3.08×10^5	2.40	3.79×10^{-3} – 7.77×10^{-3}	0.12	1.63
	SO GasEx	1.55×10^2	0.94	3.15×10^{-3} – 6.90×10^{-3}	–0.17	1.32
	Combined	1.70×10^3	1.36	2.66×10^{-3} – 7.72×10^{-3}	–0.05	1.57
$H_p k_p/2$	HiWinGS	5.98×10^2	1.27	2.53×10^{-3} – 1.67×10^{-2}	0.04	1.60
	SO GasEx	2.28×10^{-1}	–0.31	3.63×10^{-3} – 1.21×10^{-2}	–0.11	1.30
	Combined	1.23×10^2	0.91	2.37×10^{-3} – 1.67×10^{-2}	–0.10	1.56

not. Considering only the wind-sea partition of the spectrum does not improve the fits or increase the sensitivity of W to the slope estimates.

c. Combined influence of wind and wave field on whitecap coverage

The first metric considered that includes the combined effect of the wind and wave field is the wave age. The

wave age has been derived both in terms of u_* and U_{10N} as well as from the mean and peak phase speeds c_m and c_p of both the wind-sea and total spectra. As for the wave slope parameters, a nonthresholded power-law fit was computed for the various wave-age estimates (see Table 3). Shown in Fig. 11 is W plotted against the wave age expressed both in terms of U_{10N} and u_* and the peak velocity of the total and wind-sea wave field. While

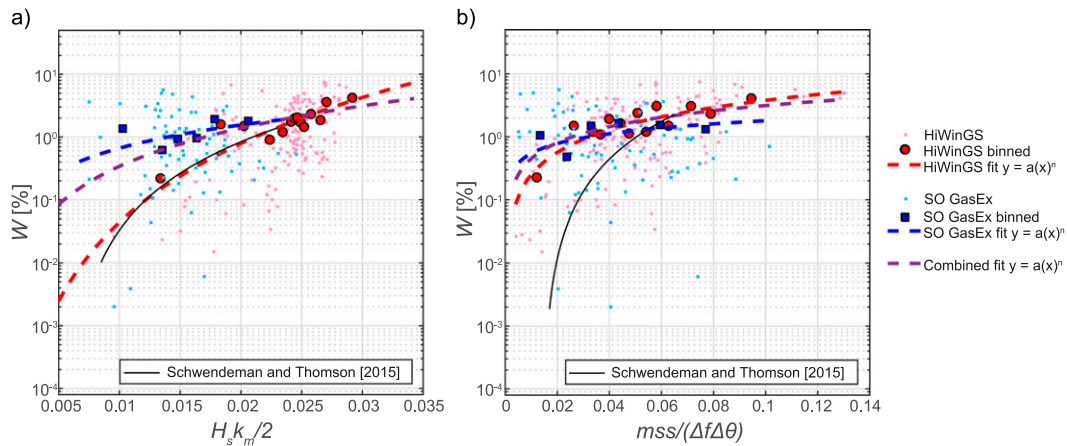


FIG. 10. Whitecap coverage W as a function of (a) mean wave steepness and (b) mean square slope normalized by the directional spread and frequency bandwidth. The small light red dots show the hourly averaged whitecap coverage computed from the HiWinGS dataset, while the small blue squares are the 30-min-averaged whitecap coverage computed from the SO GasEx dataset. The blue squares and red circles show averages of seven neighboring points for SO GasEx and HiWinGS, respectively. These are used to compute the best fit shown by the dashed red and blue lines. The dark purple lines show the best fits to the binned combined data. The black lines correspond to parameterizations of Schwendeman and Thomson (2015b).

TABLE 3. Wave-age parameterizations of whitecap coverage (%) determined in this study. Wind-sea-only statistics are denoted by a subscript. Fits and data computed as for Table 1.

Predictor	Experiment	a	n	Range	r^2	rmse
c_p/U_{10N}	HiWinGS	2.09×10^0	-1.17	0.67–2.59	0.08	1.58
	SO GasEx	1.94×10^0	-2.11	0.97–3.17	0.06	1.24
	Combined	1.96×10^0	-1.38	0.67–3.64	0.09	1.48
c_p/u_*	HiWinGS	1.76×10^2	-1.41	14.22–80.22	0.24	1.47
	SO GasEx	1.57×10^2	-1.41	21.98–79.03	-0.04	1.19
	Combined	1.57×10^2	-1.38	14.22–106.58	0.13	1.39
$c_{p_{ws}}/U_{10N}$	HiWinGS	1.92×10^0	-0.54	0.65–1.20	-0.11	1.76
	SO GasEx	7.11×10^{-1}	-1.04	0.69–1.86	-0.11	0.68
	Combined	1.58×10^0	-1.02	0.58–1.72	-0.08	1.68
$c_{p_{ws}}/u_*$	HiWinGS	2.34×10^2	-1.56	13.26–30.65	-0.01	1.63
	SO GasEx	6.65×10^0	-0.66	16.90–49.47	-0.18	0.69
	Combined	2.61×10^2	-1.63	12.14–47.78	0.04	1.54
c_m/U_{10N}	HiWinGS	1.35×10^0	-1.40	0.52–1.88	0.10	1.61
	SO GasEx	1.31×10^0	-3.64	0.81–2.27	0.30	0.98
	Combined	1.25×10^0	-1.78	0.52–2.57	0.16	1.48
c_m/u_*	HiWinGS	1.57×10^2	-1.51	10.65–57.66	0.23	1.51
	SO GasEx	2.82×10^3	-2.42	18.55–58.00	0.13	1.01
	Combined	2.25×10^2	-1.64	10.65–77.51	0.22	1.40
$c_{m_{ws}}/U_{10N}$	HiWinGS	1.77×10^0	-0.52	0.48–0.95	-0.13	1.75
	SO GasEx	5.38×10^{-1}	-2.27	0.66–1.64	0.00	0.64
	Combined	1.08×10^0	-1.42	0.41–1.51	0.00	1.64
$c_{m_{ws}}/u_*$	HiWinGS	1.26×10^2	-1.48	9.82–24.07	0.02	1.67
	SO GasEx	3.57×10^1	-1.22	16.80–43.85	-0.10	0.65
	Combined	9.99×10^1	-1.44	8.11–40.25	0.12	1.54

overall better fits were found when the wave age was expressed as a function of c_m , as was the case in Schwendeman and Thomson (2015b), plots of the wave age as a function of c_p are shown here to illustrate how the SO GasEx and HiWinGS data compare to previous studies that addressed the wave-age dependence of W .

Both datasets in Fig. 11a agree once more with that of Schwendeman and Thomson (2015b), and W is higher than reported in all other studies for a given wave age. Interestingly, when considering wind seas alone (Figs. 11b,d), the two datasets presented here no longer show matching trends, and the SO GasEx W is lower than the HiWinGS W for a given wave age. The W magnitude for a given wave age during HiWinGS is similar for the total and wind-sea-derived wave age because the wind-sea partition often contained the dominant peak. Since swell was typically dominant during SO GasEx, the change in W magnitude between total wave age and wind-sea wave age suggests less breaking occurs when a young wind sea was superimposed on swell than in an overall young sea.

The wind-wave and breaking wave Reynolds numbers are the second type of nondimensional parameters historically used to parameterize W , including both wind and sea-state dependence. When computing the wind-wave Reynolds numbers R_H , the significant H_s , mean H_m , and peak H_p wave heights were

considered. Similarly, when computing the breaking wave Reynolds number R_B , the peak ω_p and mean ω_m angular velocities were considered. Again, both the full spectrum and the wind-sea-only statistics were considered and least squares fits were used to determine nonthresholded power laws relating W to the Reynolds numbers. The viscosities were computed based on the ships' underway temperature and salinity measurements using the MATLAB Seawater Thermophysical Properties Library (Nayar et al. 2016; Sharqawy et al. 2010). Results are summarized in Tables 4 and 5. Two examples are shown in Fig. 12. Overall, the wind-wave Reynolds number fits show very good agreement between the datasets as well as with the findings of Goddijn-Murphy et al. (2011) and Scanlon and Ward (2016). The rmse between the fits determined here and for Goddijn-Murphy et al. (2011; D and E in Table A2) and for Scanlon and Ward (2016; B in Table A2) all average around 0.8%. Note that the parameterization of Zhao and Toba (2001) had to be adapted for this plot as they compute the wind-wave Reynolds number using the air viscosity rather than the water viscosity. A nominal ν_a to ν_w ratio of 11.03 was chosen. For the breaking wave Reynolds number, there is poorer agreement between datasets as well as with prior studies, though scatter appears to be reduced (c.f. r^2 in Table 5 vs. Table 4). Note again that

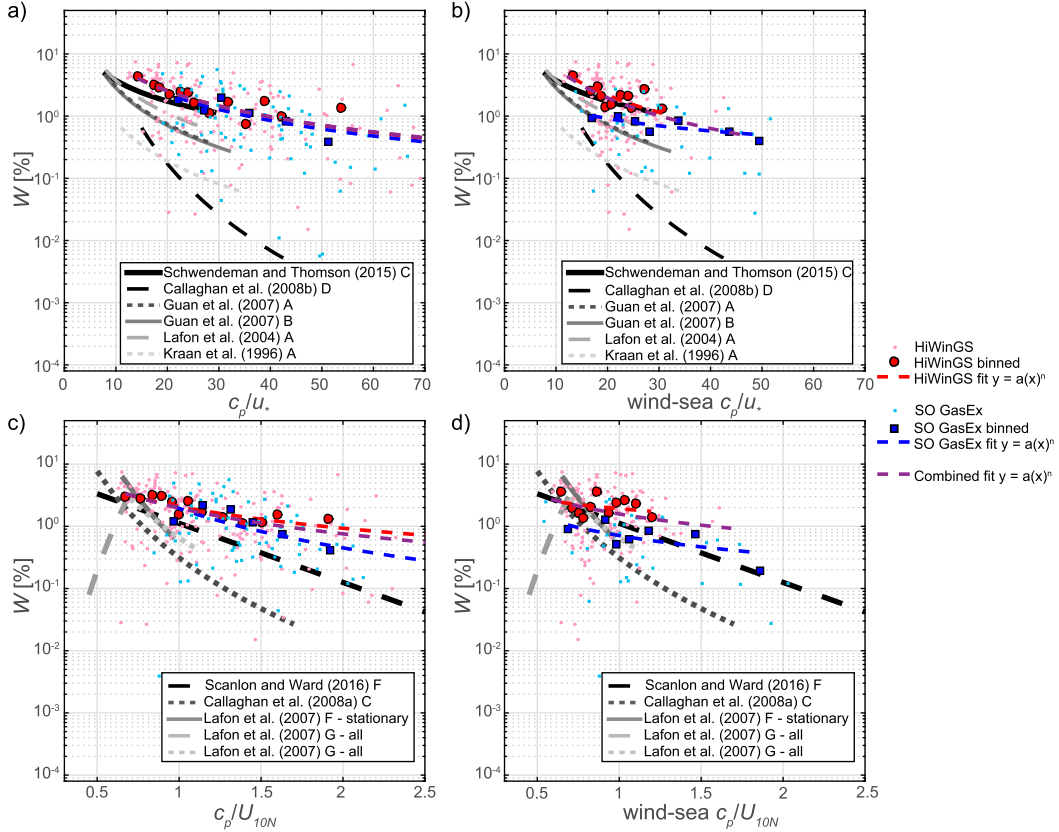


FIG. 11. Whitecap coverage W as a function of wave-age (a) c_p/u_* , (b) c_p/u_* using the wind-sea spectral peak, (c) c_p/U_{10N} using the wind-sea spectral peak, and (d) c_p/U_{10N} whitecap coverage. The small light red dots show the hourly averaged whitecap coverage computed from the HiWinGS dataset, while the small blue squares are the 30-min-averaged whitecap coverage computed from the SO GasEx dataset. The blue squares and red circles show averages of seven neighboring points for SO GasEx and HiWinGS, respectively. These are used to compute the best fit shown by the dashed red and blue lines. The dark purple lines shows the best fit to the binned, combined data. The black and gray lines correspond to the parameterizations summarized in Table A3.

previous parameterizations were adapted as the breaking Reynolds number has typically been reported in terms of the air rather than the water viscosity.

d. Multiple parameter model

As alluded to in section 4c, the dependence of W on wind and wavefield parameters can be studied through dimensionless parameters. It is apparent that W may depend on c , ρ_a , ρ_w , u_* , g , H , k , Γ , and X , where ρ_a and ρ_w are the densities of air and water, respectively; u_* is the friction velocity in air; H is a characteristic wave height; k is a characteristic wavenumber; Γ is the surface tension; and X is the wind fetch.

Considering nondimensional scaling, the whitecap coverage can be written as

$$W = f\left(\frac{\rho_a}{\rho_w}, \frac{c}{u_*}, s, \text{Re}, F, Bo\right). \quad (10)$$

Here, c/u_* is the wave age, s is a measure of the wave steepness or slope, Re is the wind-wave or breaking wave Reynolds number [see (3), (4), and (5)], F is the dimensionless fetch [$F = (gX)/c_p^2$ or $F = (gX)/u_*^2$], and Bo is the Bond number ($Bo = \Delta\rho g\Gamma^{-1}$), where g is the acceleration due to gravity. The dimensionless group ρ_a/ρ_w is approximately constant and can be ignored. As waves small enough to be directly affected by surface tension (Γ) are not resolved in the measurements, the Bond number dependence is ignored. Furthermore, not having a measure of fetch, waves will be assumed to be fetch unlimited. This leads to a simplified model

$$W = f\left(\frac{c}{u_*}, s, \text{Re}\right). \quad (11)$$

Assuming a power-law dependence of W on the nondimensional numbers, we can rewrite (11) as follows:

$$W = aX,$$

TABLE 4. Wind-wave Reynolds number parameterizations of whitecap coverage (%) determined in this study. Wind-sea-only statistics are denoted by a ws subscript. Fits and data computed as for Table 1.

Predictor	Experiment	a	n	Range	r^2	rmse
$u_* H_s / \nu_w$	HiWinGS	5.38×10^{-6}	0.88	1.95×10^5 – 4.90×10^6	0.35	1.39
	SO GasEx	3.16×10^{-8}	1.29	3.12×10^5 – 1.59×10^6	0.10	1.10
	Combined	3.21×10^{-5}	0.76	1.46×10^6 – 6.00×10^6	0.25	1.31
$u_* H_{sws} / \nu_w$	HiWinGS	2.75×10^{-4}	0.62	2.40×10^5 – 6.73×10^6	0.34	1.45
	SO GasEx	5.98×10^{-5}	0.72	2.44×10^5 – 7.24×10^5	–0.06	0.71
	Combined	9.91×10^{-5}	0.69	1.25×10^5 – 4.29×10^6	0.35	1.34
$u_* H_p / \nu_w$	HiWinGS	1.64×10^{-5}	0.82	1.45×10^5 – 3.85×10^6	0.33	1.41
	SO GasEx	8.83×10^{-8}	1.24	2.39×10^5 – 1.22×10^6	0.09	1.09
	Combined	5.65×10^{-5}	0.74	1.11×10^5 – 4.69×10^6	0.24	1.33
$u_* H_{pws} / \nu_w$	HiWinGS	3.77×10^{-4}	0.61	1.90×10^5 – 5.19×10^6	0.33	1.46
	SO GasEx	1.93×10^{-7}	1.18	2.18×10^5 – 5.88×10^5	–0.08	0.73
	Combined	7.03×10^{-5}	0.73	1.09×10^5 – 3.43×10^6	0.34	1.36
$u_* H_m / \nu_w$	HiWinGS	1.20×10^{-5}	0.91	5.50×10^4 – 1.30×10^6	0.36	1.42
	SO GasEx	2.10×10^{-7}	1.25	1.05×10^5 – 5.25×10^5	0.09	1.16
	Combined	5.80×10^{-5}	0.79	4.57×10^4 – 1.59×10^6	0.24	1.33
$u_* H_{mws} / \nu_w$	HiWinGS	4.64×10^{-4}	0.64	6.06×10^4 – 1.70×10^6	0.34	1.45
	SO GasEx	1.13×10^{-4}	0.75	5.22×10^4 – 2.30×10^5	0.04	0.74
	Combined	2.37×10^{-4}	0.70	2.15×10^4 – 1.17×10^6	0.35	1.35

where

$$X = \left(\frac{c}{u}\right)^\alpha s^\beta \text{Re}^\gamma. \quad (12)$$

The coefficients α , β , and γ can be found by minimizing a squared-difference cost function. This is done by taking the log on both sides of (12) and solving the following linear regression:

$$\log_{10} W = \log_{10} a + \alpha \log_{10} \left(\frac{c}{u}\right) + \beta \log_{10} s + \gamma \log_{10} \text{Re}. \quad (13)$$

Choosing $s = (H_m k_m)/2$, $\text{Re} = (u_* H_m)/\nu_w$, and a wave age expressed in term of the friction velocity and the mean phase speed computed from the whole wave spectrum, coefficients were computed for each dataset

individually and combined. The model determined from the combination of both datasets is shown in Fig. 13. The coefficients resulting from the linear regressions are quite different for each dataset and regressions suggest that including the steepness does not significantly improve the model (Table 6). Indeed, t -statistics suggest that $\beta = 0$ at a 91.4%, 24.7%, and 77.6% confidence level for HiWinGS, SO GasEx, and the two combined. Fit statistics ($r^2=0.52$; $\text{rmse} \sim 1.39$) suggest that multiple parameters capture more of the variability in the observed W than single-parameter, wind- and wave-dependent models. Lack of agreement between the regression results, however, does not support using a multi-nondimensional parameter model as expressed by (13). Note that both the wave age and the Reynolds numbers combine wind and wave characteristics but have opposite impacts on W . It may therefore be more

TABLE 5. Breaking wave Reynolds number parameterizations of whitecap coverage (%) determined in this study. Wind-sea-only statistics are denoted by a ws subscript. Fits and data computed as for Table 1.

Predictor	Experiment	a	n	Range	r^2	rmse
u_*^2	HiWinGS	1.85×10^{-4}	0.71	2.54×10^4 – 1.58×10^6	0.42	1.40
	SO GasEx	2.10×10^{-12}	2.09	1.66×10^5 – 6.60×10^5	0.33	0.98
	Combined	1.08×10^{-4}	0.74	2.54×10^4 – 2.04×10^6	0.24	1.34
u_*^2	HiWinGS	2.50×10^{-3}	0.52	5.47×10^4 – 1.99×10^6	0.30	1.44
	SO GasEx	4.10×10^{-6}	0.98	1.38×10^5 – 3.51×10^5	0.00	0.68
	Combined	2.24×10^{-4}	0.70	4.70×10^4 – 1.31×10^6	0.28	1.36
u_*^2	HiWinGS	2.39×10^{-4}	0.70	1.87×10^4 – 1.17×10^6	0.40	1.37
	SO GasEx	3.33×10^{-11}	1.92	1.40×10^5 – 4.77×10^5	0.33	0.93
	Combined	1.06×10^{-4}	0.76	1.87×10^4 – 1.45×10^6	0.23	1.32
u_*^2	HiWinGS	1.39×10^{-3}	0.58	4.47×10^4 – 1.49×10^6	0.31	1.42
	SO GasEx	1.93×10^{-6}	1.05	1.33×10^5 – 2.84×10^5	0.06	0.67
	Combined	1.70×10^{-4}	0.73	4.15×10^4 – 9.62×10^5	0.24	1.36

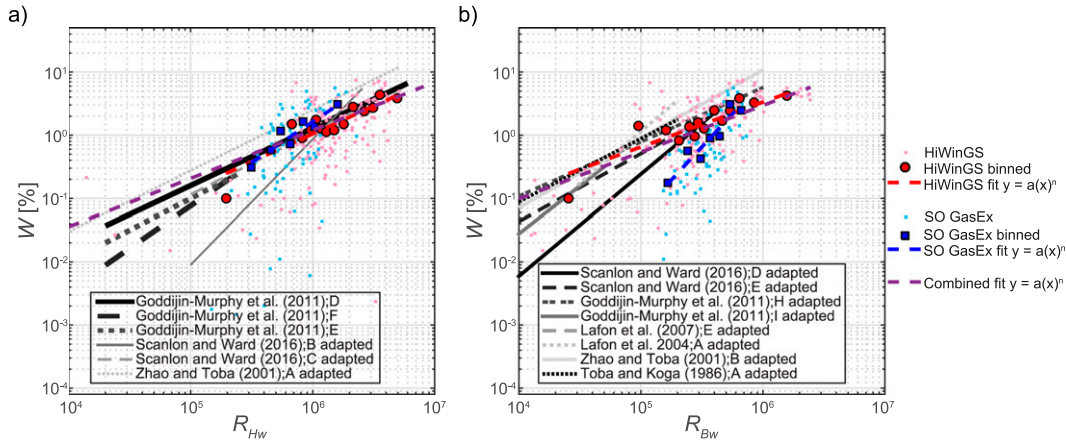


FIG. 12. Whitecap coverage W as a function of (a) wave-wind and (b) breaking wave Reynolds number computed from the significant wave height and peak angular velocity of the entire wave spectrum. The small light red dots show the hourly averaged whitecap coverage computed from the HiWinGS dataset, while the small blue squares are the 30-min-averaged whitecap coverage computed from the SO GasEx dataset. The blue squares and red circles show averages of seven neighboring points for SO GasEx and HiWinGS, respectively. These are used to compute the best fit shown by the dashed red and blue lines. The dark purple lines shows the best fit to the binned combined data. The black and gray lines correspond to the parameterizations summarized in Table A2.

physically intuitive to combine only one of these two nondimensional numbers with the pure sea-state parameter that is steepness. However, statistically, combining only two nondimensional numbers rather than three led to poorer results. As the Reynolds numbers capture most of the variance of W of the nondimensional numbers considered here, $W(s, Re)$ is a better model than $W(s, clu)$.

5. Discussion

Careful considerations need to be made before using parameterizations beyond their range of validity. Extrapolations, while often unavoidable, increase uncertainties and may lead to erroneous results. Ongoing efforts and targeted field campaigns allow for an ever-wider range of environmental conditions to be sampled, and a combined dataset will lead to more precise and universal parameterizations. New parameterizations should clearly state the range for which they are valid. This was done for the results reported here and as far as possible for the parameterizations compiled from the existing literature.

Prior studies not only differ in the whitecap detection algorithms used but also in the application of appropriate image projection and scaling. To evaluate the impact of image scaling on the whitecap coverage estimate, we compared results from SO GasEx computed with or without scaling. For a given frame, image scaling significantly alters W ; however, when computing 20-min-averaged W , the impact of scaling appears to average out. The scaling has minimal impact when considering over 6000 frames, as illustrated in Fig. 14. Recording attitude angles and

georectifying images is therefore not essential when computing W but is critical when tracking breakers, such as for determining the breaking crest length distribution.

When considering wind speed only (Fig. 9a) and wind-wave Reynolds number (Fig. 12a) parameterizations, the level of agreement between the two datasets analyzed in this study with existing parameterizations is remarkable.

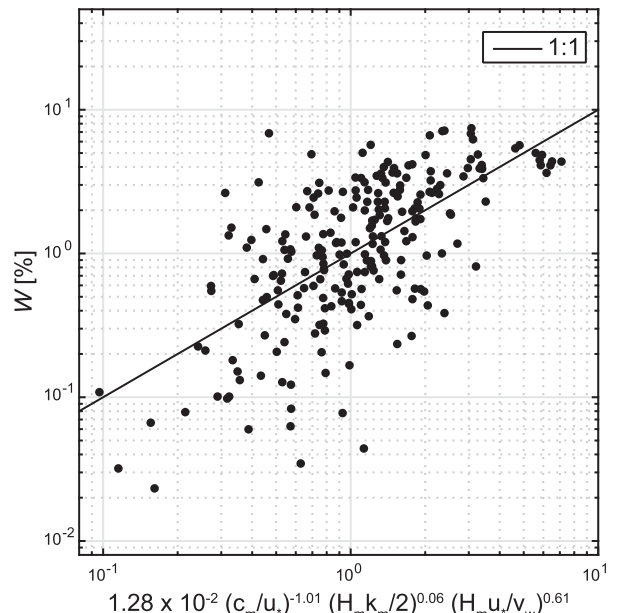


FIG. 13. Scatterplot of the measured whitecap coverage W plotted against the multiple parameter model: $W = a(c_m u_*)^\alpha [(H_m k_m)/2]^\beta [(H_m u_*)/v_w]^\gamma$. The 1:1 line is in black.

TABLE 6. Result of the linear regression $\log_{10} W = \log_{10} a + \alpha \log_{10}(c_m/u_*) + \beta \log_{10}[(H_s k_m)/2] + \gamma \log_{10}(H_m u_* / \nu_w)$.

Experiment		Estimate	<i>t</i> -statistics	<i>p</i> -value
HiWinGS	<i>a</i>	1.43×10^{-4}	-2.56	1.13×10^{-2}
	α	-0.77	-3.73	2.62×10^{-4}
	β	-0.03	-0.11	9.14×10^{-1}
	γ	0.86	5.32	3.53×10^{-7}
SO GasEx	<i>a</i>	7.52×10^{-5}	-1.16	2.51×10^{-1}
	α	-1.33	-2.42	1.85×10^{-2}
	β	-0.66	-1.17	2.47×10^{-1}
	γ	0.82	2.25	2.77×10^{-2}
Combined	<i>a</i>	1.28×10^{-2}	-1.84	6.72×10^{-2}
	α	-1.01	-5.44	1.40×10^{-7}
	β	0.06	0.29	7.76×10^{-1}
	γ	0.61	5.30	2.77×10^{-7}

Close agreement between these two datasets and recently published parameterizations give confidence in the recently developed and now commonly used thresholding technique, and it may be valuable to reanalyze old datasets with the same method if possible. The additional step of removing background gradients before running the AWE (section 3a) ensures removal of biases arising from varying light conditions and camera exposure and brightness settings. A similar approach was put forward by Mironov and Dulov (2008). Agreement between the WW3 hindcast wave statistics and in situ observations is also remarkable (Fig. 8). This should encourage reanalysis of wave-dependent whitecap parameterizations for earlier datasets using hindcasts to complement measurements and to evaluate them over a wider range of conditions.

Recent wind speed–only total whitecap parameterizations show less scatter for intermediate to high wind

speeds than previously suggested (Anguelova and Webster 2006). When considered within their originally defined wind speed range, they fall within 30% of their average, spanning an order of magnitude, for $U_{10} > 10 \text{ m s}^{-1}$. Note that the datasets presented here are much larger than those obtained from previous field experiments. Therefore, a larger amount of variability may be expected. Indeed, the data presented here display variability similar to that of the combined historical datasets (cf. Albert et al. 2016; Fig. 1), which is greater than reported in individual studies. Significant scatter of up to two orders of magnitude remains in hourly W observations at many wind speeds, and further studies are necessary to thoroughly understand it. While surfactants have been shown to prolong the lifetime of foam at the water surface (e.g., Garrett 1967; Callaghan et al. 2016) and their spatial inhomogeneity may account for some of the observed scatter for a given wind speed and sea state, they are difficult to measure under wind speeds greater than 10 m s^{-1} (Cunliffe and Wurl 2014). Technological development and more observations are evidently needed.

Targeted sampling under high winds and young sea conditions during HiWinGS extended the upper limit of the validity range for wind-only whitecap parameterizations to 25 m s^{-1} . It is important to note here that unlike the majority of previous studies, the neutral 10-m wind speed U_{10N} was considered here. While mostly stable conditions were encountered during SO GasEx, this was not the case during HiWinGS. Both Goddijn-Murphy et al. (2011) and Salisbury et al. (2013) used equivalent neutral winds and therefore, maybe not

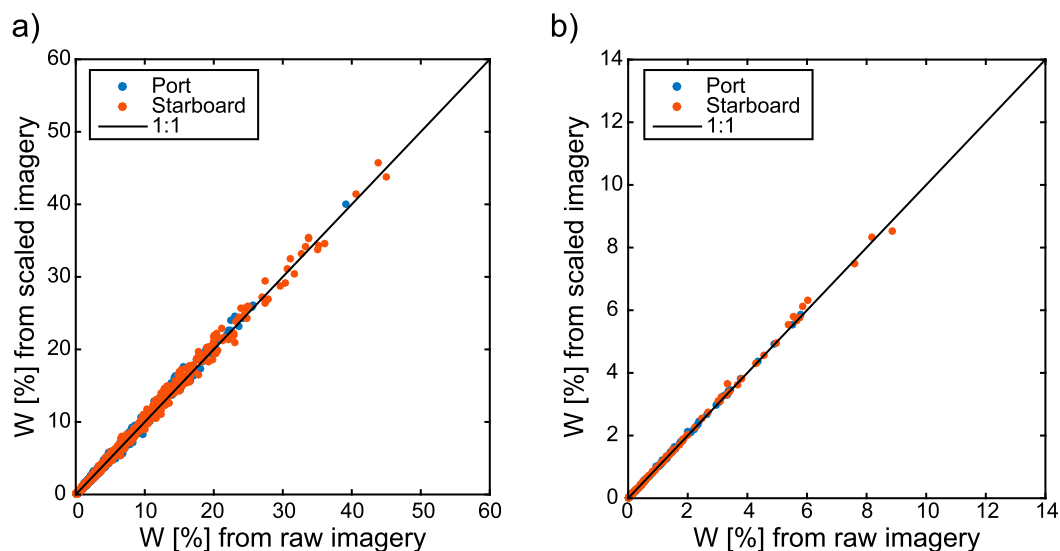


FIG. 14. Scatterplots of the whitecap coverage W estimated from the scaled and nonscaled imagery: (a) individual frames and (b) 20-min averages.

surprisingly, match the parameterizations determined in the current study the best. The neutral wind speed and friction velocity along with nondimensional numbers calculated from them are the only quantities that account for varying atmospheric stability conditions and therefore allow for true comparison from one dataset to the next. The differences in whitecap parameterizations arising from the stability dependence and correction has been evaluated by [Paget et al. \(2015\)](#).

As hinted at by [Schwendeman and Thomson \(2015b\)](#) and [Callaghan et al. \(2008b\)](#), W is seen to level off at high wind speed (cf. [Fig. 1](#) and [Fig. 9a](#)), not exceeding 10% when averaged over a 20-min to hourly period. To evaluate W saturation at high winds, linear fits were performed through the high wind speed data points, and t -tests were used to determine if the slopes were significantly different than zero. The t -tests reveal that for $U_{10N} > 18 \text{ m s}^{-1}$ (26 hourly averages), the slope of W versus U_{10N} is significantly different than zero only at a 14% confidence level; that is, W is near constant. If the lower wind speed bound is reduced to 17.5 m s^{-1} , the confidence that the slope is significantly different than zero is raised to 74% and for $U_{10N} > 17 \text{ m s}^{-1}$, it is at 92%. Analysis of a very small number of visible images of the sea surface taken under hurricanes equally implied that W remains near constant for $U_{10} > 24 \text{ m s}^{-1}$ ([Holthuijsen et al. 2012](#)). Note that under high wind speeds, streaks of foam and especially spray dominate, and [Holthuijsen et al. \(2012\)](#) did not include streaks in their W estimate, making it more representative of the active whitecap coverage than the total coverage considered here. Widespread spray coverage at high wind speed may render whitecap and streak detection more difficult in imagery. There may therefore be a practical upper wind speed limit to the current image analysis technique.

The datasets analyzed here display weaker wind speed dependence than most previous studies, except for [Salisbury et al. \(2013\)](#). This weak wind speed dependence of W may be attributed to the low sea surface temperatures, averaging around 5° – 8°C , in which most of the measurements were taken. Only during the last station during HiWinGS did temperature exceed 10°C while surface water temperatures during SO GasEX did not exceed 14°C . Early work by [Monahan and O'Muircheartaigh \(1986\)](#) provided evidence of a weaker dependence of W on wind speed U for SSTs of 16°C compared to 32°C , but the increase of W with SST at a given wind speed was found to be modest. They analyzed five datasets, including that collected by [Bortkovskii \(1987\)](#), which displays a strong positive dependence of W on SST and a near-linear dependence of W on wind speed for SST less than 3°C . [Monahan and O'Muircheartaigh \(1986\)](#) argued that the water temperature will impact the exponent of the $W(U)$ power law and suggested that for SSTs around 10°C , the

exponent is around 2, while for SSTs warmer than 22°C the exponent is greater than 3. The weaker wind speed dependence in cold waters is reflected in the latitudinal variation of the dependence of W on U shown by [Monahan et al. \(2015\)](#), which is supported by [Salisbury et al. \(2014\)](#), who demonstrated that using a power-law wind speed dependence with an exponent of 3.41 leads to overestimation of W at high latitudes. [Wu \(1988\)](#) suggested that rather than affecting the exponent, temperature affects a , the slope of the power-law equation [(2)], though no systematic trends were found. It was further argued that all coefficients of the power law vary with temperature, with the strongest temperature dependence in the exponent ([Albert et al. 2016](#)). Cold waters suppress the rate of breaking but increase the lifetime of bubbles and foam patches thus having the potential to enhance or reduce W ([Bortkovskii and Novak 1993](#)). Opposite trends in temperature dependence of air entrainment have been found in laboratory studies ([Hwang et al. 1991](#); [Salter et al. 2014](#); [Callaghan et al. 2014](#)). As individual field campaigns rarely sample a wide range of environmental parameters, it is essential to compile all existing data to detect trends, and caution is advisable in determining trends from reduced datasets.

Continued improvement of whitecap parameterizations requires consideration of more than wind speed, specifically including statistics of the variable wave field. This motivated the concurrent measurement of whitecaps, winds, and wave field during SO GasEX and HiwinGS. Purely wave-dependent parameterizations that express W as a function of wave steepness or mean square slope within the equilibrium range do not give improved results over the wind speed-only parameterizations nor does the wave-age parameterization provide a better fit. The wind-wave Reynolds number-based parameterizations show tighter correlations and better interdataset agreement than wave age- and wave-only parameterizations. More wind and sea-state conditions should be sampled to establish any limitations to these relationships. The breaking Reynolds number captures more of the variability in individual datasets, but R_{B_w} displays less interdataset agreement. Reynolds number functions have also been shown to provide better models of sea spray aerosol fluxes than wind speed alone, with R_H explaining twice as much of the total variance in direct measurements ([Norris et al. 2013](#)). While the Reynolds numbers have been typically computed using the friction velocity, the HiWinGS and SO GasEX data suggest that using the neutral 10-m wind speed lead to similar fit statistics for W .

Energy-weighted or mean statistics f_m , H_m , k_m , and c_m are regularly chosen as being more representative of the breaking waves rather than peak statistics f_p , H_p , k_p , and c_p , which often correspond to the swell in multimodal spectra ([Sutherland and Melville 2015](#)). [Schwendeman](#)

and Thomson (2015b) show that mean statistics are better predictors for W parameterizations, further encouraging their use. The use of energy-weighted statistics of the wind-sea partition was motivated by the observation that most whitecaps are associated with waves even shorter than the mean (Gemrich et al. 2008). This study, however, only suggests marginal improvement of fit statistics using mean wavefield statistics.

As stated in the introduction, mss is computed over the equilibrium range. The existence of such a range, where sources and sinks are in balance was postulated by Phillips (1985). Based on measurements by Toba (1973), Phillips (1985) proposed an analytical expression for the energy spectrum within that range, which is characterized by a f^{-4} spectral shape. Bounds for the equilibrium range were later suggested by Donelan (1985) as $1.5f_p$ and $3.5f_p$. The upper bounds, however, seemed to be dictated by the highest-frequency resolved by the measurements rather than the end of the range in which the spectrum is proportional to f^{-4} . Indeed, the equilibrium range was found to extend further: up to $6f_p$ (Toba 1973) or 0.35 to 0.4 Hz in Thomson et al. (2013) for f_p generally less than 0.1 Hz. Furthermore, the upper limit of the equilibrium range is not always easily detectable, with no visible shift in slope of $E(f)$ at the transition between the equilibrium and the saturation ranges.

The SO GasEx and HiWinGS datasets suggest that for multimodal spectra, particularly when the winds increase and wind seas start appearing, $1.5f_p < f < 3.5f_p$ incorporates the wind-sea peak, while $\sqrt{2}f_m \leq f \leq \sqrt{5}f_m$ usually falls beyond the wind-sea peak. This is illustrated in Fig. 7d. What is more, the equilibrium range defined in terms of f_m also extends to higher frequencies, and its upper limit falls within those observed by Thomson et al. (2013). Determining the equilibrium range based on sections of the spectra beyond f_p that most closely decays as f^{-4} led to highly variable results with little agreement between WW3 and the Waverider. The mss computed over that range showed less correlation with W than the mss computed over $\sqrt{2}f_m \leq f \leq \sqrt{5}f_m$.

Finally, alignment of the swell and the wind sea was considered during the analysis by differentiating between periods of pure wind sea and pure swell as well as following, cross, and counter swell as defined in Sugihara et al. (2007). This analysis did not, however, result in distinct trends for the different alignments and is consequently not shown here.

6. Conclusions

Analysis of visible imagery, flux, and wave data collected during SO GasEx and HiWinGS allowed for evaluation of existing whitecap coverage parameterizations.

Considering the two datasets separately and computing best fits for each individually facilitates critical assessment of the parameterizations discussed in this study, which are further verified by comparison to published parameterizations. Based on this work and recent studies reviewed herein, it is apparent that wind speed-only parameterizations show very little scatter for winds above 10 m s^{-1} and are able to capture the observed variability of W well. The neutral wind speed or friction velocity should be used for those parameterizations. Of all the wave-only and wind- and wave-dependent parameterizations tested here, the wind-wave Reynolds number parameterizations appear to be the most universally applicable ones, as suggested by the close agreement between the best fits determined from the individual and combined datasets, which are further in good agreement with those of Goddijn-Murphy et al. (2011) and Scanlon and Ward (2016). Although wind-wave Reynolds number parameterizations capture somewhat less of the observed variability in W , they are in closer agreement to previous studies than wind-only parameterizations. When wavefield statistics are readily available, wind-wave Reynolds number parameterizations should be used. Such statistics do not have to be derived from directional spectra as separating wind seas from swell does not appear to yield significantly better representation of W . Results from this study do not support a more complex multiparameter whitecap coverage model based on non-dimensional scaling.

Acknowledgments. This work was funded by the National Science Foundation (Grants OCE-0647667, OCE-1537890, AGS-1036062, AGS-1036006, and AGS-1444294), the National Oceanic and Atmospheric Administration (Grant NA07OAR4310094), and the Natural Environment Research Council (Grant NE/J020893/1). The authors thank the anonymous reviewers for thoroughly and critically evaluating the manuscript. They are also grateful to the crew of the R/V *Knorr* for supporting us while chasing storms and that of the NOAA ship *Ronald H. Brown* for their support during SO GasEx. Data from the HiWinGS cruise will be made available via anonymous ftp (ftp1.esrl.noaa.gov/psd3/cruises/HIWINGS_2013/Collective_Archive). The SO GasEX data can be found online (at <http://www.bco-dmo.org/project/2064>).

APPENDIX

Summary of Whitecap Coverage Parameterizations before 2017

Previous parameterizations of whitecap coverage are presented in Tables A1–A4.

TABLE A1. Parameterizations of whitecap coverage (%) as a function of wind speed (since 2004). Letters given in the second column are used as references in the legends in Fig. 1.

Reference	Eq.	Formula	Wind speed range (m s^{-1})	Sea state	Dataset
Scanlon and Ward (2016)	A	$W(U_{10}) = 7.84 \times 10^{-4}(U_{10\text{NW}} - 2.56)^3$	$1 < U_{10} \leq 21$		R/V Knorr 2011 (Knorr11) and Surface Ocean Aerosol Production (SOAP) 2012 North Pacific cruises 2012 and 2015
Schwendeman and Thomson (2015b)	A	$W(U_{10}) = 2.81 \times 10^{-3}(U_{10\text{NW}} - 3.87)^{2.76}$	$5.5 < U_{10} \leq 16$		
Salisbury et al. (2013)	A	$W_{10}(U_{10}) = 4.6 \times 10^{-3} U_{10}^{1.26}$	$2 < U_{10} \leq 20$		Satellite W, 10 Ghz
	B	$W_{37}(U_{10}) = 3.97 \times 10^{-2} U_{10}^{2.59}$			Satellite W, 37 Ghz
Goddijn-Murphy et al. (2011)	A	$W(U_{10}) = 15.9 \times 10^{-4} U_{10}^{2.7}$	$4.6 < U_{10} < 23.09$		Marine Aerosol Production (MAP) campaign W; in situ winds
	B	$W(U_{10}) = 35.7 \times 10^{-4}(U_{10} - 3.83)^3$	$U_{10} < 11.5$		
Callaghan et al. (2008a)	C	$W(U_{10}) = 46.9 \times 10^{-5}(U_{10} + 2.28)^3$	$U_{10} > 9.25$		Coastal site at Martha's Vineyard
	A	$W(U_{10}) = 4.66 \times 10^{-5} U_{10}^{3.95}$	$3.5 < U_{10} < 12$	Mixed seas	
	B	$W(U_{10}) = 2.99 \times 10^{-5} U_{10}^{3.95}$	$3.5 < U_{10} < 12$	Swell dominated	
Callaghan et al. (2008b)	A	$W(U_{10}) = 3.18 \times 10^{-3}(U_{10} - 3.7)^3$	$4.6 < U_{10} \leq 11.25$		MAP campaign
	B	$W(U_{10}) = 4.82 \times 10^{-4}(U_{10} + 1.98)^3$	$9.25 < U_{10} \leq 23.09$		
Sugihara et al. (2007)	A	$W(U_{10}) = 8.04 \times 10^{-4}(U_{10} - 2.01)^3$	$4.37 < U_{10} < 16.35$	All	Shirahama observation tower
	B	$W(U_{10\text{NW}}) = 8.57 \times 10^{-4}(U_{10\text{NW}} - 1.34)^3$	$4.79 < U_{10\text{NW}} < 16.57$	Pure wind sea	
Lafon et al. (2007)	C	$W(U_{10\text{NW}}) = 1.09 \times 10^{-3}(U_{10\text{NW}} - 3.24)^3$	$4.79 < U_{10\text{NW}} < 16.57$	Other	Etat de Mer et Modélisation de l'Aérosol
	A	$W(U_{10}) = 8.1 \times 10^{-5} U_{10}^{3.88}$	$10 \leq U_{10} \leq 17.9$	Stationary	(EMMA) campaign Toulon-Hyeres Bay
	B	$W(U_{10}) = 1.9 \times 10^{-4} U_{10}^{3.51}$		All	

TABLE A2. Parameterizations of whitecap coverage (%) as a function of breaking wave and wind-wave Reynolds numbers. Letters given in the second column are used as references in the legends in Fig. 12.

Reference	Eq.	Formula	Range	Dataset and comments
Scanlon and Ward (2016)	B	$W(R_{H_s}) = 1.1 \times 10^{-10} R_{H_s}^{1.98} (\log\text{-logfit})$	$10^4 < R_{H_s} < 2.5 \times 10^5$	Knorr11 and SOAP 2012
	C	$W(R_{H_s}) = 1.4 \times 10^{-5} R_{H_s}^{0.98}$		
	D	$W(R_{B_s}) = 8.9 \times 10^{-8} R_{B_s}^{0.61} (\log\text{-logfit})$	$2.1 \times 10^2 < R_{B_s} < 7 \times 10^4$	
Goddijn-Murphy et al. (2011)	E	$W(R_{B_s}) = 2.7 \times 10^{-5} R_{B_s}^{1.07}$		
	D	$W(R_{H_{sw}}) = 4.51 \times 10^{-6} R_{H_{sw}}^{0.91}$	$2 \times 10^4 < R_{H_{sw}} < 6 \times 10^6$	
	E	$W(R_{H_{sw}}) = 10.2 \times 10^{-7} R_{H_{sw}}^{1.4}$	$2 \times 10^4 < R_{H_{sw}} < 2.5 \times 10^5$	
	F	$W(R_{H_{sw}}) = 1.53 \times 10^{-8} R_{H_{sw}}^{1.34}$	$2 \times 10^4 < R_{H_{sw}} < 2.5 \times 10^5 (U_{10} < 8.6)$	MAP W; in situ wind; ECMWF wave stats $R_{H_{sw}}$ computed based on wind-sea H_s
	G	$W(R_{H_{sw}}) = 11.3 \times 10^{-7} R_{H_{sw}}^{0.95}$		
	H	$W(R_{B_s}) = 28.6 \times 10^{-5} R_{B_s}^{0.86}$	$3 \times 10^2 < R_{B_s} < 10^5$	
	I	$W(R_{B_s}) = 8.28 \times 10^{-7} R_{B_s}^{1.51}$	$3 \times 10^2 < R_{B_s} < 5 \times 10^3 (U_{10} < 8.6)$	
Lafon et al. (2007)	E	$W(R_{H_s}) = 3.7 \times 10^{-2} R_{H_s}^{1.1}$	$6 \times 10^3 < R_{H_s} < 3 \times 10^4$	EMMA campaign Toulon-Hyeres Bay
	A	$W(R_{B_s}) = 3.2 \times 10^{-7} R_{B_s}^{1.64}$	$3 \times 10^3 < R_{B_s} < 2 \times 10^4$	Flux, Etat de mer, et Télédetection en Condition de Fetch (FETCH) variable
Zhao and Toba (2001)	A	$W(R_{H_s}) = 4.02 \times 10^{-5} R_{H_s}^{0.96}$	$10^2 \leq R_{H_s} \leq 5 \times 10^5$	Wind-wave tunnel, coastal and other field data from six different studies
Toba and Koga (1986)	B	$W(R_{B_s}) = 3.88 \times 10^{-5} R_{B_s}^{1.09}$	$10^2 \leq R_{B_s} < 10^5$	Wind-wave tunnel and oceanographic tower
	A	$W(R_{B_s}) = 8.9 \times 10^{-5} R_{B_s}^{0.9}$	$5 \times 10^2 < R_{B_s} < 2 \times 10^4$	

TABLE A3. Parameterizations of whitecap coverage (%) as a function of wave age. Letters given in the second column are used as references in the legends in Fig. 11.

Reference	Eq.	Formula	Range	Datasets
Scanlon and Ward (2016)	F	$W\left(\frac{c_p}{U_{10}}\right) = 9.97\left(\frac{c_p}{U_{10}}\right)^{-0.95}$	$1 \leq \frac{c_p}{U_{10}} \leq 6$	Knorr11 and SOAP 2012
Schwendeman and Thomson (2015b)	C	$W\left(\frac{c_p}{u_*}\right) = 47\left(\frac{c_p}{u_*}\right)^{-1.1}$	$8 < \frac{c_p}{u_*} < 29$	
	D	$W\left(\frac{c_m}{U_{10}}\right) = 8.48 \times 10^{-1}\left(\frac{c_m}{U_{10}}\right)^{-3.53}$		North Pacific cruises 2012 and 2015
	E	$W\left(\frac{c_m}{u_*}\right) = 9.33 \times 10^2\left(\frac{c_m}{u_*}\right)^{-1.945}$	$18 < \frac{c_m}{u_*} < 52$	
Callaghan et al. (2008a)	C	$W\left(\frac{c_p}{U_{10}}\right) = 3.11 \times 10^{-2}\left(\frac{c_p}{U_{10}}\right)^{-4.63}$	$0.5 \leq \frac{c_p}{U_{10}} \leq 1.7$	Coastal site at Martha's Vineyard
	D	$W\left(\frac{c_p}{u_*}\right) = 1.81 \times 10^5\left(\frac{c_p}{u_*}\right)^{-4.63}$	$15 \leq \frac{c_p}{u_*} \leq 48$	
Guan et al. (2007)	A	$W\left(\frac{c_p}{u_*}\right) = 2.97 \times 10^2\left(\frac{c_p}{u_*}\right)^{-2}$	$8 < \frac{c_p}{u_*} < 28$	FETCH
	B	$W\left(\frac{c_p}{u_*}\right) = 2.82 \times 10^2\left(\frac{c_p}{u_*}\right)^{-2}$	$8 < \frac{c_p}{u_*} < 32$	FETCH and Bohai Sea datasets
Lafon et al. (2007)	F	$W\left(\frac{c_p}{u_{10}}\right) = 0.54 \times \left(\frac{c_p}{U_{10}}\right)^{-5.75}$	$0.67 \leq \frac{c_p}{U_{10}} < 1$ $0.52 \leq \frac{c_p}{U_{10}} \leq 0.69$	EMMA campaign Toulon-Hyeres Bay
	G	$W\left(\frac{c_p}{U_{10}}\right) = \begin{cases} 70 \times \left(\frac{c_p}{U_{10}}\right)^{8.5} \\ 0.65 \times \left(\frac{c_p}{U_{10}}\right)^{-4.1} \end{cases}$	$0.69 < \frac{c_p}{U_{10}} < 1$	
	B	$W\left(\frac{c_p}{u_*}\right) = 210\left(\frac{c_p}{u_*}\right)^{-1.75}$	$15 < \frac{c_p}{u_*} < 28$	FETCH
Lafon et al. (2004)	C	$W\left(\frac{c_p}{u_*}\right) = 2 \times 10^6\left(\frac{c_p}{u_*}\right)^{-4.9}$	$8 < \frac{c_p}{u_*} < 28$	
	D	$W\left(\frac{c_p}{u_*}\right) = -0.187 \times \left(\frac{c_p}{u_*}\right) + 5.2$	$8 < \frac{c_p}{u_*} < 28$	
	A	$W_A\left(\frac{c_p}{u_*}\right) = 96\left(\frac{c_p}{u_*}\right)^{-2.08}$	$11 \leq \frac{c_p}{u_*} \leq 34$	Air Sea Gas Exchange (ASGASEX) and Meetpost Noordwijk coastal research platform

TABLE A4. Parameterizations of whitecap coverage (%) as a function of the friction velocity u_* . Letters given in the second column are used as references in the legends in Fig. 9b.

Reference	Eq.	Formula	Wind speed range (m s^{-1})	Sea-state conditions	Dataset
Schwendeman and Thomson (2015b)	B	$W(u_*) = 6.82(u_* - 1.39 \times 10^{-1})^{2.04}$	$0.2 < u_* \leq 0.75$	Stationary all	North Pacific cruises 2012 and 2015
Sugihara et al. (2007)	D	$W(u_*) = 9.53(u_* - 0.074)^3$	$0.212 < u_* < 0.67$		Shirahama observation tower
Lafon et al. (2007)	C	$W(u_*) = 10.2u_*^{2.53}$	$0.33 \leq u_* \leq 0.8$		EMMA campaign Toulon-Hyeres Bay
	D	$W(u_*) = 7.78u_*^{2.29}$			

REFERENCES

- Albert, M. F. M. A., M. D. Angelova, A. M. M. Manders, M. Schaap, and G. de Leeuw, 2016: Parameterization of oceanic whitecap fraction based on satellite observations. *Atmos. Chem. Phys.*, **16**, 13 725–13 751, doi:10.5194/acp-16-13725-2016.
- Andreae, M. O., and D. Rosenfeld, 2008: Aerosol–cloud–precipitation interactions. Part 1. The nature and sources of cloud-active aerosols. *Earth Sci. Rev.*, **89**, 13–41, doi:10.1016/j.earscirev.2008.03.001.
- Angelova, M. D., and F. Webster, 2006: Whitecap coverage from satellite measurements: A first step toward modeling the variability of oceanic whitecaps. *J. Geophys. Res.*, **111**, C03017, doi:10.1029/2005JC003158.
- Asher, W. E., and R. Wanninkhof, 1998: The effect of bubble-mediated gas transfer on purposeful dual-gaseous tracer experiments. *J. Geophys. Res.*, **103**, 10 555–10 560, doi:10.1029/98JC00245.
- , and Coauthors, 1995: Measurement of gas transfer, whitecap coverage, and brightness temperature in a surf pool: An overview of WABEX-93. *Proc. Third Int. Symp. on Air-Water Gas Transfer*, Heidelberg, Germany, Image Processing, 205–216.
- Banner, M. L., J. R. Gemmrich, and D. M. Farmer, 2002: Multiscale measurements of ocean wave breaking probability. *J. Phys. Oceanogr.*, **32**, 3364–3375, doi:10.1175/1520-0485(2002)032<3364:MMOOWB>2.0.CO;2.
- Blanchard, D. C., 1963: The electrification of the atmosphere by particles from bubbles in the sea. *Prog. Oceanogr.*, **1**, 73–202, doi:10.1016/0079-6611(63)90004-1.
- , 1983: The production, distribution, and bacterial enrichment of the sea-salt aerosol. *Air-Sea Exchange of Gases and Particles*, P. S. Liss and W. G. N. Slinn, Eds., Springer, 407–454.
- Blomquist, B. W., C. W. Fairall, B. J. Huebert, D. J. Kieber, and G. R. Westby, 2006: DMS sea-air transfer velocity: Direct measurements by eddy covariance and parameterization based on the NOAA/COARE gas transfer model. *Geophys. Res. Lett.*, **33**, L07601, doi:10.1029/2006GL025735.
- Bobak, J. P., W. E. Asher, D. J. Dowgiallo, and M. D. Angelova, 2011: Aerial radiometric and video measurements of whitecap coverage. *IEEE Trans. Geosci. Remote Sens.*, **49**, 2183–2193, doi:10.1109/TGRS.2010.2103565.
- Bortkovskii, R. S., 1987: *Air-Sea Exchange of Heat and Moisture during Storms*. Dordrecht, 193 pp.
- , and V. A. Novak, 1993: Statistical dependencies of sea state characteristics on water temperature and wind-wave age. *J. Mar. Syst.*, **4**, 161–169, doi:10.1016/0924-7963(93)90006-8.
- Bouquet, J.-Y., 2015: Camera calibration toolbox for MATLAB. California Institute of Technology. [Available online at http://www.vision.caltech.edu/bouquetj/calib_doc/.]
- Callaghan, A. H., and M. White, 2009: Automated processing of sea surface images for the determination of whitecap coverage. *J. Atmos. Oceanic Technol.*, **26**, 383–394, doi:10.1175/2008JTECHO634.1.
- , G. B. Deane, and M. D. Stokes, 2008a: Observed physical and environmental causes of scatter in whitecap coverage values in a fetch-limited coastal zone. *J. Geophys. Res.*, **113**, C05022, doi:10.1029/2007JC004453.
- , G. D. Leeuw, L. Cohen, and C. D. O’Dowd, 2008b: Relationship of oceanic whitecap coverage to wind speed and wind history. *Geophys. Res. Lett.*, **35**, L23609, doi:10.1029/2008GL036165.
- , M. D. Stokes, and G. B. Deane, 2014: The effect of water temperature on air entrainment, bubble plumes, and surface foam in a laboratory breaking-wave analog. *J. Geophys. Res. Oceans*, **119**, 7463–7482, doi:10.1002/2014JC010351.
- , G. B. Deane, and M. D. Stokes, 2016: Laboratory air-entraining breaking waves: Imaging visible foam signatures to estimate energy dissipation. *Geophys. Res. Lett.*, **43**, 11 320–11 328, doi:10.1002/2016GL071226.
- Cavaleri, L., and Coauthors, 2007: Wave modelling—The state of the art. *Prog. Oceanogr.*, **75**, 603–674, doi:10.1016/j.pocean.2007.05.005.
- , B. Fox-Kemper, and M. Hemer, 2012: Wind waves in the coupled climate system. *Bull. Amer. Meteor. Soc.*, **93**, 1651–1661, doi:10.1175/BAMS-D-11-00170.1.
- Cifuentes-Lorenzen, A., J. B. Edson, C. J. Zappa, and L. Bariteau, 2013: A multi-sensor comparison of ocean wave frequency spectra from a research vessel during the Southern Ocean Gas Exchange Experiment. *J. Atmos. Oceanic Technol.*, **30**, 2907–2925, doi:10.1175/JTECH-D-12-00181.1.
- Cunliffe, M., and Coauthors, 2014: Guide to best practices to study the ocean’s surface. Scientific Committee on Oceanic Research Sea Surface Microlayer Working Group Rep., 118 pp.
- de Leeuw, G., E. L. Andreas, M. D. Angelova, C. W. Fairall, E. R. Lewis, C. O’Dowd, M. Schulz, and S. E. Schwartz, 2011: Production flux of sea spray aerosol. *Rev. Geophys.*, **49**, RG2001, doi:10.1029/2010RG000349.
- Donelan, M. A., 1985: Directional spectra of wind-generated waves. *Philos. Trans. Roy. Soc. London*, **A315**, 509–562, doi:10.1098/rsta.1985.0054.
- Edson, J. B., A. A. Hinton, K. E. Prada, J. E. Hare, and C. W. Fairall, 1998: Direct covariance flux estimates from mobile platforms at sea. *J. Atmos. Oceanic Technol.*, **15**, 547–562, doi:10.1175/1520-0426(1998)015<0547:DCFEFM>2.0.CO;2.
- , C. J. Zappa, J. Ware, W. R. McGillis, and J. E. Hare, 2004: Scalar flux profile relationships over the open ocean. *J. Geophys. Res.*, **109**, C08S09, doi:10.1029/2003JC001960.
- , and Coauthors, 2011: Direct covariance measurement of CO₂ gas transfer velocity during the 2008 Southern Ocean Gas Exchange Experiment: Wind speed dependency. *J. Geophys. Res.*, **116**, C00F10, doi:10.1029/2011JC007022.
- , and Coauthors, 2013: On the exchange of momentum over the open ocean. *J. Phys. Oceanogr.*, **43**, 1589–1610, doi:10.1175/JPO-D-12-0173.1.
- Fairall, C. W., E. F. Bradley, J. E. Hare, A. A. Grachev, and J. B. Edson, 2003: Bulk parameterization of air–sea fluxes: Updates and verification for the COARE algorithm. *J. Climate*, **16**, 571–591, doi:10.1175/1520-0442(2003)016<0571:BPOASF>2.0.CO;2.
- , and Coauthors, 2011: Implementation of the Coupled Ocean–Atmosphere Response Experiment flux algorithm with CO₂, dimethyl sulfide, and O₃. *J. Geophys. Res.*, **116**, C00F09, doi:10.1029/2010JC006884.
- Farmer, D. M., C. L. McNeil, and B. D. Johnson, 1993: Evidence for the importance of bubbles in increasing air–sea gas flux. *Nature*, **361**, 620–623, doi:10.1038/361620a0.
- Frew, N. M., 1997: The role of organic films in air–sea gas exchange. *The Sea Surface and Global Change*, P. S. Liss and R. A. Duce, Eds., Cambridge University Press, 121–172.
- Frouin, R., S. F. Iacobellis, and P. Y. Deschamps, 2001: Influence of oceanic whitecaps on the global radiation budget. *Geophys. Res. Lett.*, **28**, 1523–1526, doi:10.1029/2000GL012657.
- Gaiser, P. W., and Coauthors, 2004: The WindSat spaceborne polarimetric microwave radiometer: Sensor description and early orbit performance. *IEEE Trans. Geosci. Remote Sens.*, **42**, 2347–2361, doi:10.1109/TGRS.2004.836867.

- Garrett, W. D., 1967: Stabilization of air bubbles at the air-sea interface by surface active material. *Deep-Sea Res. Oceanogr. Abstr.*, **14**, 661–672, doi:10.1016/S0011-7471(67)80004-4.
- Gemmrich, J. R., M. L. Banner, and C. Garrett, 2008: Spectrally resolved energy dissipation and momentum flux of breaking waves. *J. Phys. Oceanogr.*, **38**, 1296–1312, doi:10.1175/2007JPO3762.1.
- Goddijn-Murphy, L., D. K. Woolf, and A. H. Callaghan, 2011: Parameterizations and algorithms for oceanic whitecap coverage. *J. Phys. Oceanogr.*, **41**, 742–756, doi:10.1175/2010JPO4533.1.
- Gordon, H. R., and M. Wang, 1994: Retrieval of water-leaving radiance and aerosol optical thickness over the oceans with SeaWiFS: A preliminary algorithm. *Appl. Opt.*, **33**, 443–452, doi:10.1364/AO.33.000443.
- Guan, C., W. Hu, J. Sun, and R. Li, 2007: The whitecap coverage model from breaking dissipation parameterizations of wind waves. *J. Geophys. Res.*, **112**, C05031, doi:10.1029/2006JC003714.
- Hanson, J. L., and O. M. Phillips, 1999: Wind sea growth and dissipation in the open ocean. *J. Phys. Oceanogr.*, **29**, 1633–1648, doi:10.1175/1520-0485(1999)029<1633:WSGADI>2.0.CO;2.
- , and —, 2001: Automated analysis of ocean surface directional wave spectra. *J. Atmos. Oceanic Technol.*, **18**, 277–293, doi:10.1175/1520-0426(2001)018<0277:AAOOSD>2.0.CO;2.
- Hasselmann, S., K. Hasselmann, J. H. Allender, and T. P. Barnett, 1985: Computations and parameterizations of the nonlinear energy transfer in a gravity-wave spectrum. Part II: Parameterizations of the nonlinear energy transfer for application in wave models. *J. Phys. Oceanogr.*, **15**, 1378–1391, doi:10.1175/1520-0485(1985)015<1378:CAPOTN>2.0.CO;2.
- Haywood, J. M., V. Ramaswamy, and B. J. Soden, 1999: Tropospheric aerosol climate forcing in clear-sky satellite observations over the oceans. *Science*, **283**, 1299–1303, doi:10.1126/science.283.5406.1299.
- Ho, D. T., and Coauthors, 2011: Southern Ocean Gas Exchange Experiment: Setting the stage. *J. Geophys. Res.*, **116**, C00F08, doi:10.1029/2010JC006852.
- Holland, K. T., R. A. Holman, T. C. Lippmann, J. Stanley, and N. Plant, 1997: Practical use of video imagery in nearshore oceanographic field studies. *IEEE J. Oceanic Eng.*, **22**, 81–92, doi:10.1109/48.557542.
- Holthuijsen, L. H., M. D. Powell, and J. D. Pietrzak, 2012: Wind and waves in extreme hurricanes. *J. Geophys. Res.*, **117**, C09003, doi:10.1029/2012JC007983.
- Hwang, P. A., Y. Poon, and J. Wu, 1991: Temperature effects on generation and entrainment of bubbles induced by a water jet. *J. Phys. Oceanogr.*, **21**, 1602–1605, doi:10.1175/1520-0485(1991)021<1602:TEOGAE>2.0.CO;2.
- Jessup, A. T., C. J. Zappa, M. R. Loewen, and V. Hesany, 1997: Infrared remote sensing of breaking waves. *Nature*, **385**, 52–55, doi:10.1038/385052a0.
- Johnson, D., 2012: DIWASP: Directional wave spectra toolbox for MATLAB: User manual. Research Rep. WP-1601-DJ (V1.1), 21 pp.
- Kleiss, J. M., and W. K. Melville, 2010: Observations of wave breaking kinematics in fetch-limited seas. *J. Phys. Oceanogr.*, **40**, 2575–2604, doi:10.1175/2010JPO4383.1.
- Komen, G. J., L. Cavaleri, M. A. Donelan, K. Hasselmann, S. Hasselmann, and P. A. E. M. Janssen, 1994: *Dynamics and Modelling of Ocean Waves*. Cambridge University Press, 532 pp.
- Kraan, G., W. A. Oost, and P. A. E. M. Janssen, 1996: Wave energy dissipation by whitecaps. *J. Atmos. Oceanic Technol.*, **13**, 262–267, doi:10.1175/1520-0426(1996)013<0262:WEDBW>2.0.CO;2.
- Kuik, A. J., G. P. van Vledder, and L. H. Holthuijsen, 1988: A method for the routine analysis of pitch-and-roll buoy wave data. *J. Phys. Oceanogr.*, **18**, 1020–1034, doi:10.1175/1520-0485(1988)018<1020:AMFTRA>2.0.CO;2.
- Lafon, C., J. Piazzola, P. Forget, O. Le Calve, and S. Despiau, 2004: Analysis of the variations of the whitecap fraction as measured in a coastal zone. *Bound.-Layer Meteor.*, **111**, 339–360, doi:10.1023/B:BOUN.0000016490.83880.63.
- , —, —, and S. Despiau, 2007: Whitecap coverage in coastal environment for steady and unsteady wave field conditions. *J. Mar. Syst.*, **66**, 38–46, doi:10.1016/j.jmarsys.2006.02.013.
- Lund, B., C. J. Zappa, H. C. Graber, and A. Cifuentes-Lorenzen, 2017: Shipboard wave measurements in the Southern Ocean. *J. Atmos. Oceanic Technol.*, doi:10.1175/JTECH-D-16-0212.1, in press.
- Melville, W. K., 1996: The role of surface-wave breaking in air-sea interaction. *Annu. Rev. Fluid Mech.*, **28**, 279–321, doi:10.1146/annurev.fl.28.010196.001431.
- Mironov, A. S., and V. A. Dulov, 2008: Detection of wave breaking using sea surface video records. *Meas. Sci. Technol.*, **19**, 015405, doi:10.1088/0957-0233/19/1/015405.
- Monahan, E. C., 1971: Oceanic whitecaps. *J. Phys. Oceanogr.*, **1**, 139–144, doi:10.1175/1520-0485(1971)001<0139:OW>2.0.CO;2.
- , 1993: Occurrence and evolution of acoustically relevant subsurface bubble plumes and their associated, remotely monitorable, surface whitecaps. *Natural Physical Sources of Underwater Sound: Sea Surface Sound (2)*, B. R. Kerman, Ed., Springer Netherlands, 503–517, doi:10.1007/978-94-011-1626-8_37.
- , and M. C. Spillane, 1984: The role of oceanic whitecaps in air-sea gas exchange. *Gas Transfer at Water Surfaces*, W. Brutsaert and G. H. Jirka, Eds., D. Reidel, 495–503.
- , and I. G. O’Muircheartaigh, 1986: Whitecaps and the passive remote sensing of the ocean surface. *Int. J. Remote Sens.*, **7**, 627–642, doi:10.1080/01431168608954716.
- , G. Hooker, and C. J. Zappa, 2015: The latitudinal variation in the wind-speed parameterization of oceanic whitecap coverage: Implications for global modelling of air-sea gas flux and sea surface aerosol generation. *19th Conf. on Air-Sea Interaction*, Phoenix, AZ, Amer. Meteor. Soc., 14.5. [Available online at <https://ams.confex.com/ams/95Annual/webprogram/Paper260446.html>.]
- Mori, N., T. Suzuki, and S. Kakuno, 2007: Noise of acoustic Doppler velocimeter data in bubbly flows. *J. Eng. Mech.*, **133**, 122–125, doi:10.1061/(ASCE)0733-9399(2007)133:1(122).
- Myrhaug, D., and L. E. Holmedal, 2008: Effects of wave age and air stability on whitecap coverage. *Coastal Eng.*, **55**, 959–966, doi:10.1016/j.coastaleng.2008.03.005.
- Nayar, K. G., M. H. Sharqawy, L. D. Banchik, and J. H. Lienhard V, 2016: Thermophysical properties of seawater: A review and new correlations that include pressure dependence. *Desalination*, **390**, 1–24, doi:10.1016/j.desal.2016.02.024.
- Norris, S. J., I. M. Brooks, and D. J. Salisbury, 2013: A wave roughness Reynolds number parameterization of the sea spray source flux. *Geophys. Res. Lett.*, **40**, 4415–4419, doi:10.1002/grl.50795.
- Paget, A. C., M. A. Bourassa, and M. D. Angelova, 2015: Comparing in situ and satellite-based parameterizations of oceanic whitecaps. *J. Geophys. Res. Oceans*, **120**, 2826–2843, doi:10.1002/2014JC010328.

- Phillips, O. M., 1985: Spectral and statistical properties of the equilibrium range in wind-generated gravity waves. *J. Fluid Mech.*, **156**, 505–531, doi:10.1017/S0022112085002221.
- Randolph, K., H. M. Dierssen, A. Cifuentes-Lorenzen, W. Balch, E. C. Monahan, C. Zappa, D. Drapeau, and B. Bowler, 2017: Novel methods for optically measuring whitecaps under natural wave breaking conditions in the Southern Ocean. *J. Atmos. Oceanic Technol.*, **34**, 533–554, doi:10.1175/JTECH-D-16-0086.1.
- Saha, S., and Coauthors, 2010: The NCEP Climate Forecast System Reanalysis. *Bull. Amer. Meteor. Soc.*, **91**, 1015–1057, doi:10.1175/2010BAMS3001.1.
- Salisbury, D. J., M. D. Anguelova, and I. M. Brooks, 2013: On the variability of whitecap fraction using satellite-based observations. *J. Geophys. Res. Oceans*, **118**, 6201–6222, doi:10.1002/2013JC008797.
- , —, and —, 2014: Global distribution and seasonal dependence of satellite-based whitecap fraction. *Geophys. Res. Lett.*, **41**, 1616–1623, doi:10.1002/2014GL059246.
- Salter, M. E., E. D. Nilsson, A. Butcher, and M. Bilde, 2014: On the seawater temperature dependence of the sea spray aerosol generated by a continuous plunging jet. *J. Geophys. Res. Atmos.*, **119**, 9052–9072, doi:10.1002/2013JD021376.
- Scanlon, B., and B. Ward, 2013: Oceanic wave breaking coverage separation techniques for active and maturing whitecaps. *Methods Oceanogr.*, **8**, 1–12, doi:10.1016/j.mio.2014.03.001.
- , and —, 2016: The influence of environmental parameters on active and maturing oceanic whitecaps. *J. Geophys. Res. Oceans*, **121**, 3325–3336, doi:10.1002/2015JC011230.
- Schwendeman, M., and J. Thomson, 2015a: A horizon-tracking method for shipboard video stabilization and rectification. *J. Atmos. Oceanic Technol.*, **32**, 164–176, doi:10.1175/JTECH-D-14-00047.1.
- , and —, 2015b: Observations of whitecap coverage and the relation to wind stress, wave slope, and turbulent dissipation. *J. Geophys. Res. Oceans*, **120**, 8346–8363, doi:10.1002/2015JC011196.
- , —, and J. R. Gemmrich, 2014: Wave breaking and dissipation in a young wind sea. *J. Phys. Oceanogr.*, **44**, 104–127, doi:10.1175/JPO-D-12-0237.1.
- Sharqawy, M. H., J. H. Lienhard, and S. M. Zubair, 2010: Thermophysical properties of seawater: A review of existing correlations and data. *Desalin. Water Treat.*, **16**, 354–380, doi:10.5004/dwt.2010.1079.
- Spillane, M., E. C. Monahan, P. Bowyer, D. Doyle, and P. J. Stabenro, 1986: Whitecaps and global fluxes. *Oceanic Whitecaps*, Springer, 209–218.
- Stokes, G. G., 1880: Considerations relative to the greatest height of oscillatory irrotational waves which can be propagated without change of form. *Math. Phys. Pap.*, **1**, 225–228.
- Sugihara, Y., H. Tsumori, T. Ohga, H. Yoshioka, and S. Serizawa, 2007: Variation of whitecap coverage with wave-field conditions. *J. Mar. Syst.*, **66**, 47–60, doi:10.1016/j.jmarsys.2006.01.014.
- Sutherland, P., and W. K. Melville, 2015: Field measurements of surface and near-surface turbulence in the presence of breaking waves. *J. Phys. Oceanogr.*, **45**, 943–965, doi:10.1175/JPO-D-14-0133.1.
- Thomson, J., E. D’Asaro, M. Cronin, W. Rogers, R. Harcourt, and A. Shcherbina, 2013: Waves and the equilibrium range at Ocean Weather Station P. *J. Geophys. Res. Oceans*, **118**, 5951–5962, doi:10.1002/2013JC008837.
- Toba, Y., 1973: Local balance in the air-sea boundary processes. *J. Oceanogr. Soc. Japan*, **29**, 209–220, doi:10.1007/BF02108528.
- , and M. Koga, 1986: A parameter describing overall conditions of wave breaking, whitecapping, sea-spray production and wind stress. *Oceanic Whitecaps*, E. Monahan and G. Niocaill, Eds., Springer, 37–47.
- Tolman, H. L., 2009: User manual and system documentation of WAVEWATCH III TM version 3.14. U.S. Department of Commerce/NOAA/NWS/NCEP Tech. Note, MMAB 276, 220 pp.
- , and D. Chalikov, 1996: Source terms in a third-generation wind wave model. *J. Phys. Oceanogr.*, **26**, 2497–2518, doi:10.1175/1520-0485(1996)026<2497:STIATG>2.0.CO;2.
- , B. Balasubramanian, L. D. Burroughs, D. V. Chalikov, Y. Y. Chao, H. S. Chen, and V. M. Gerald, 2002: Development and implementation of wind-generated ocean surface wave models at NCEP. *Wea. Forecasting*, **17**, 311–333, doi:10.1175/1520-0434(2002)017<0311:DAIOWG>2.0.CO;2.
- Wallace, D. W. R., and C. D. Wirick, 1992: Large air-sea gas fluxes associated with breaking waves. *Nature*, **356**, 694–696, doi:10.1038/356694a0.
- Wolf, D. K., 1997: Bubbles and their role in air-sea gas exchange. *The Sea Surface and Global Change*, P. S. Liss and R. Duce, Eds., Cambridge University Press, 173–206.
- , 2005: Parameterization of gas transfer velocities and sea-state-dependent wave breaking. *Tellus*, **57B**, 87–94, doi:10.3402/tellusb.v57i2.16783.
- , and Coauthors, 2007: Modelling of bubble-mediated gas transfer: Fundamental principles and a laboratory test. *J. Mar. Syst.*, **66**, 71–91, doi:10.1016/j.jmarsys.2006.02.011.
- Wu, J., 1988: Variations of whitecap coverage with wind stress and water temperature. *J. Phys. Oceanogr.*, **18**, 1448–1453, doi:10.1175/1520-0485(1988)018<1448:VOWCWW>2.0.CO;2.
- Zappa, C. J., M. L. Banner, J. R. Gemmrich, H. Schultz, R. P. Morison, D. A. LeBel, and T. Dickey, 2012: An overview of sea state conditions and air-sea fluxes during RaDyO. *J. Geophys. Res.*, **117**, C00H19, doi:10.1029/2011JC007336.
- Zhao, D., and Y. Toba, 2001: Dependence of whitecap coverage on wind and wind-wave properties. *J. Oceanogr.*, **57**, 603–616, doi:10.1023/A:1021215904955.